Morpho-structural evolution of the Cordón Caulle geothermal region, Southern Volcanic Zone, Chile: Insights from gravity and $^{40}Ar/^{39}Ar$ dating

Fabián Sepúlveda[a,*], Alfredo Lahsen[a], Sylvain Bonvalot[b,c], José Cembrano[d], Antonia Alvarado[a], Pablo Letelier[a]

[a]*Departmento de Geología, Universidad de Chile, P.O. Box 13518, (21) Santiago, Chile*
[b]*Departmento de Geofísica, Universidad de Chile, Blanco Encalada 2085, Santiago, Chile*
[c]*Institut de Recherche pour le Développement (IRD), Unité de Recherche 154, France*
[d]*Departmento de Ciencias Geológicas, Universidad Católica del Norte, Avda. Angamos 0610, Antofagasta, Chile*

Abstract

The Cordón Caulle geothermal region (40.5°S) is a 13 km × 6 km, NW-SE elongate, volcano-tectonic depression hosting numerous monogenetic volcanic centers, fumaroles, and hot-springs, most of which occur spatially associated with the edges of the depression. Volcanism started at approximately 0.3 Ma, with dominantly mafic effusions, and expressed ultimately in post-glacial and historic dacite–rhyolite eruptions (1921–1922 and 1960). Three NE-trending gravimetric profiles were carried out across the depression of Cordón Caulle, yielding a residual negative anomaly with the greatest amplitude (−20 mGal) at the center of the depression. A 2D-gravity model given by a 490 m thick shallow body with a density contrast = −650 kg/m^3, interpreted as a shallow package of dacite–rhyolite lavas and tephra, was found to match the residual anomaly. A dense rock equivalent volume of felsic material on the order of 28 km^3 (25% of the total output of Cordón Caulle) is derived from this thickness. Previous workers explain the origin of felsic rocks at Cordón Caulle in terms of the orientation of the borders of Cordón Caulle relative to the maximum stress direction σ_1 (i.e. NE-trending) prevailing during the Quaternary, according to which NW-trending domains were compressional, favoring stagnation, storage and differentiation of magmas. The dominantly monogenetic style of volcanism, the plateau-like morphology and the negative Bouguer anomaly, on the contrary, are interpreted as an indication of extensional tectonics. Intra-arc extension is proposed to be related to coseismic or postseismic stress relaxation accompanying major thrust events, such as the great 1960 Chilean earthquake, which is consistent, at Cordón Caulle, with the direction of propagation of dikes of the 1960 eruption (i.e. coseismic extension) and present-day subsidence inferred from InSAR data (i.e. postseismic extension). Prior to the Quaternary (8.2–1.6 Ma), nearly east-west compression prevailed at the intra-arc zone. A 5.44 ± 0.04 Ma old granodiorite intrusion bracketed by two sub-parallel branches of the regional, margin-parallel Liquiñe–Ofqui Fault Zone (LOFZ) in a prominent pop-up structure, 15 km to the east of Cordón

* Corresponding author.
E-mail address: fsepulve@cec.uchile.cl (F. Sepúlveda).

Caulle, accounts for reverse reactivation of the LOFZ and rapid fault-related exhumation of basement rocks (>1 mm/year). We argue that under compression, reverse reactivation of the LOFZ was facilitated by the combined effect of cyclic increase in fluid pressure induced by magmatic–hydrothermal input, and removal of lithostatic load induced by glacial erosion (>1.5 mm/year in the vicinity of Cordón Caulle).

Keywords: geothermal; gravity; oblique domain; coseismic; interseismic; postseismic; reactivation; Cordón Caulle; Chile; Andes

1. Introduction

The Chilean Andes host one of the largest undeveloped geothermal provinces of the world. The volcanic-geothermal activity in the Chilean Andes is primarily controlled by the convergence of the Nazca and South American Plates. Since 5 Ma, the Nazca plate motion vector has remained relatively constant at an angle of 22° (N78°E) to the normal to the plate boundary, with convergence rates in the range of 65–110 mm/year at 40°S (Pardo-Casas and Molnar, 1987; Somoza, 1998; Angermann et al., 1999; Fig. 1a). The Quaternary volcanic arc includes two active segments, namely, the Central Volcanic Zone (CVZ; 17–28°S) and the Southern Volcanic Zone (SVZ; 33–46°S). The segmentation of the volcanic arc is attributed to anisotropies in the geometry of the Wadati–Benioff zone (Cahill and Isaacks, 1992). The segmentation of the arc is accompanied by along-strike changes in crustal thickness (up to 70 km along the CVZ; about 38 km along the SVZ) and composition (felsic-dominated along the CVZ; mafic-dominated along the SVZ; Tassara, 1997; Tassara et al., 2004).

A long-lived, first-order anisotropy of the SVZ is represented by the 1000 km long, NNE-trending Liquiñe–Ofqui Fault Zone (LOFZ; Cembrano et al., 1996, 2000, 2002; Fig. 1). In this study, we define the LOFZ as an *arc-parallel* domain. The majority of the Quaternary stratovolcanoes (39–46°S), as well as several hot spring areas (e.g. Oporto, Baños de Cupido, Baños de Chiu-Chiu, Rupanco and Callao; Pérez, 1999) occur in the vicinity of the LOFZ (Fig. 1b).

On a more local scale, the SVZ is intersected by second-order anisotropies with NW and NE orientation (Cembrano and Moreno, 1994; López-Escobar et al., 1995). In this study, we refer to these anisotropies as *oblique* domains (Fig. 1b). Some stratovolcanoes such as Puyehue and Casablanca (~40°S; Fig. 1b and 2) lie over the junction of arc-parallel and oblique domains. Some of the largest geothermal systems of the SVZ, among which are Nevados de Chillán (36.9°S; Lahsen, 1978; Dixon et al., 1999) and Cordón Caulle (40.5°S; Moreno, 1977; Fig. 1b), are related to NW-trending Late-Pleistocene volcanic silicic complexes, with multiple surface manifestations accounting for several hundreds of megawatts thermal (MWt) (e.g. ~100 MWt in Nevados de Chillán; ~40 MWt in Cordón Caulle; Sepúlveda and Lahsen, 2003; Sepúlveda et al., 2004a,b).

Between 37° and 42°S, NE-trending domains are typified by the alignment of monogenetic, post-glacial basaltic scoria cones, as seen in the Carrán–Los Venados (40.3°S), Mencheca (40.5°S) and Casablanca (40.8°S) groups (Fig. 1b and 2), and by the alignment of polygenetic cones, as seen in Los Cenizos Fissure (41°S; Fig. 1b). NE-trending domains are rarely associated with geothermal activity.

In spite of the remarkable morphological expression of arc-parallel and oblique domains throughout the Cordón Caulle geothermal region (Fig. 2), kinematic indicators are largely concealed either by dense vegetation or superimposed volcanism. In this paper, we present a multiple approach including gravity, $^{40}Ar/^{39}Ar$ dating and Al-in-hornblende geobarometry, aimed at better understanding the Late Miocene to Present nature of these structures and their reactivation pattern relative to the prevailing stress regime.

2. Late Miocene to Present tectonic-structural setting of the SVZ

Based on kinematic and seismic data, Lavenu and Cembrano (1999) outlined two main tectonic events for the intra-arc zone (37–42°S): a Late Miocene to Pliocene (between 8.2 and 1.6 Ma) compressional event with east-west-oriented σ_1, and a Quaternary dextral transpressional regime with northeast-oriented

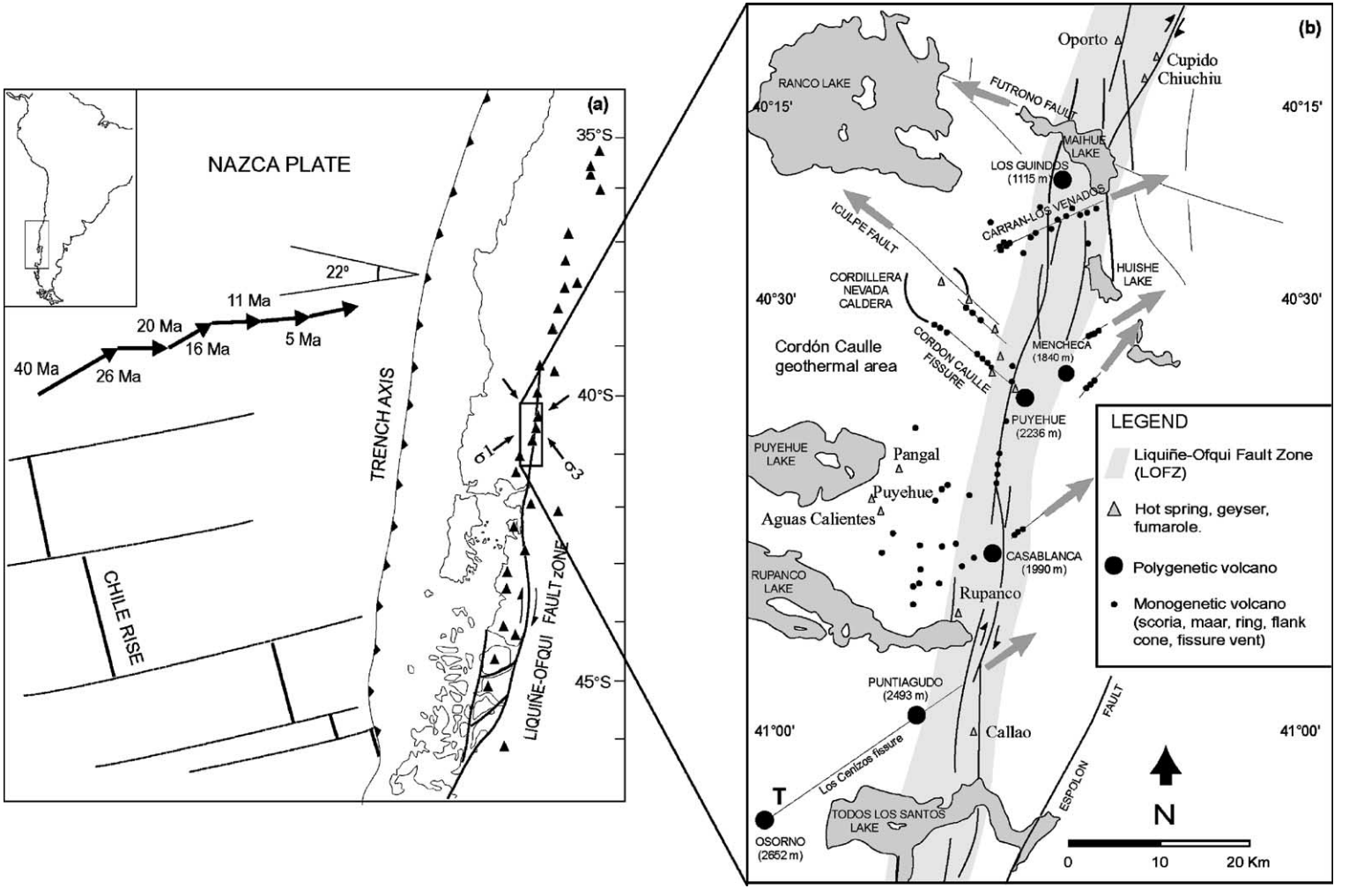

Fig. 1. (a) Tectonic setting of the Andean Southern Volcanic Zone (33–46°S), showing the Liquiñe–Ofqui Fault Zone System (LOFZ), the plate motion vector since the last 40 Ma (in arrows; Somoza, 1998), the current direction of plate convergence (22° to the normal to the plate boundary), and the Quaternary stress field prevailing in the intra-arc zone (37–42°S; Lavenu and Cembrano, 1999). (b) Structural sketch (40–41°S) highlighting the LOFZ main trend (with a component of dextral strike-slip motion extensively documented; Cembrano et al., 1996, 2000, 2002) and oblique domains (in gray arrows).

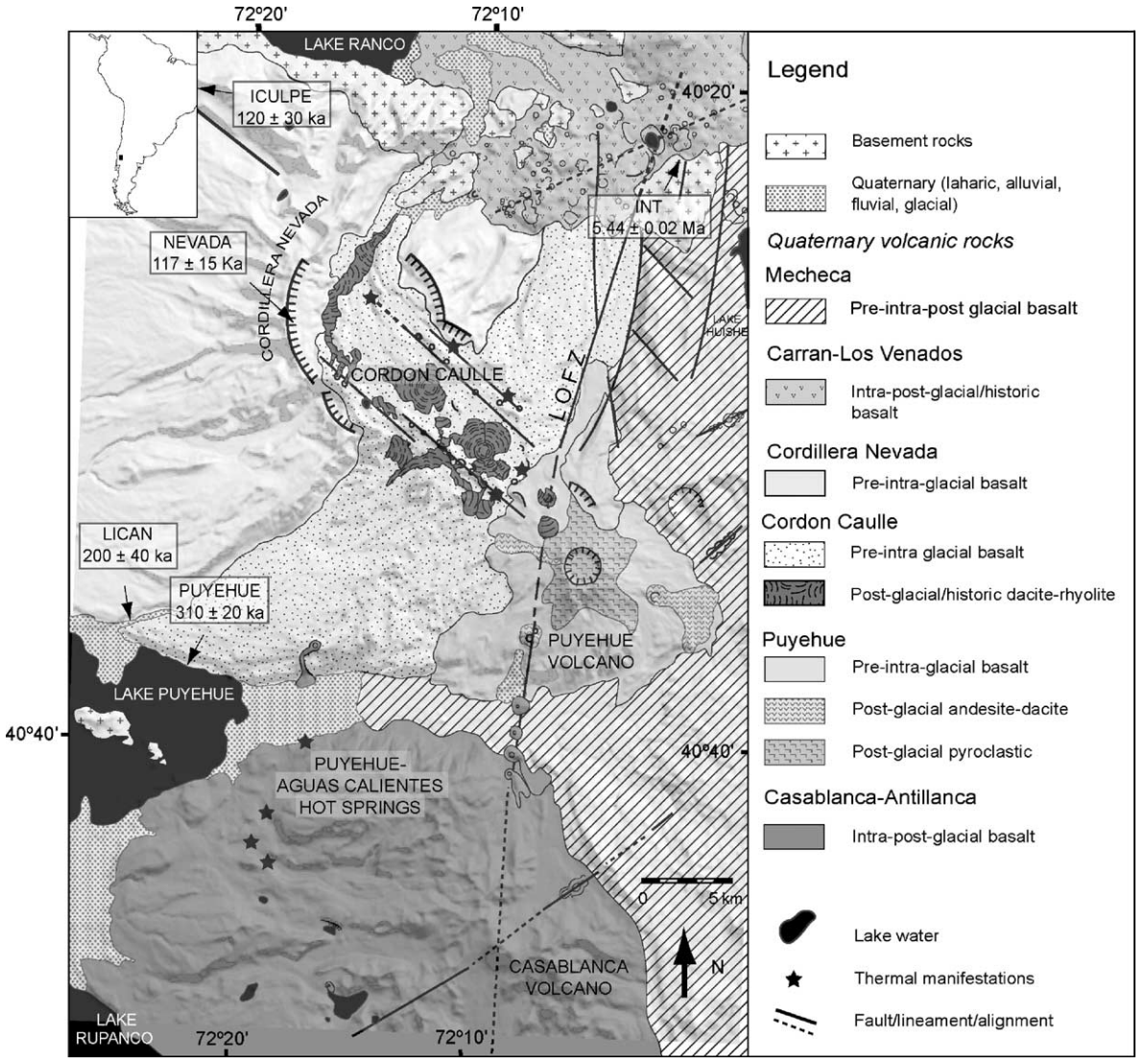

Fig. 2. Geological map of the Cordón Caulle area (after Moreno, 1977) showing $^{40}Ar/^{39}Ar$ ages obtained in this study. Pre-glacial = older than 100 ka; intra-glacial = 100–10 ka old; post-glacial = younger than 10 ka.

σ_1 (younger than 1.6 Ma; Fig. 1a). The long-term σ_1 direction not parallel to the plate convergence vector has been interpreted in terms of both oblique subduction and the collision of the Chile Rise against South-America (Forsythe and Nelson, 1985; Thomson, 2002). Present-day shortening of the continental border (26–37°S), roughly parallel to the plate convergence vector, has been documented by GPS stations (Klotz et al., 2001), suggesting interseismic strain accumulation related to dextral transpression, due to locking of the interplate contact. The amount of shortening (up to 3.5 cm/year) progressively decreases from the trench to the east. Between 37–42°S, GPS velocity vectors distribute in a non-uniform fashion, which has been attributed to *post-seismic* deformation following the Great 1960 Chilean Earthquake (Klotz et al., 2001).

Pre-Late Cretaceous motion, as well as Miocene and Pliocene right-lateral strike-slip and dextral-reverse displacements have been documented along

the LOFZ (Cembrano et al., 1996, 2000, 2002). Exhumation rates in the range of 1.3–2.7 mm/year, commencing between approximately 7 to 4 Ma, were estimated close to the southernmost termination of the LOFZ (42–46°S), based on thermocronological–geobarometric data (Parada et al., 2000) and fission-tracks ages of apatite and zircon (Thomson, 2002). Similarly, presently-exposed ductile shear zones of the LOFZ (mean Ar–Ar age of 4 Ma; Cembrano et al., 1996, 2000, 2002) allowed Cembrano et al. (2002) to arrive at exhumation rates of 1.8 mm/year, by assuming a vertical exhumation range of ~7 km (~350 °C) and a thermal gradient of 50 °C/km. The recognition of Late-Miocene intrusions and Pliocene mylonites along the LOFZ has suggested fault-related exhumation to these workers.

NW-trending anisotropies have been ascribed to faults inherited from the basement, probably previous to the Cenozoic Andean cycle (Cembrano and Moreno, 1994). Between 39° and 42°S, the long-lived character of NW-trending domains is suggested by the existence of NW-oriented plutonic belts of Paleozoic and Jurassic age (Munizaga et al., 1988). At Cordón Caulle, NW-trending anisotropies extend to the northwest through the Iculpe Valley (Fig. 1b and 2), beyond the perimeter of the Quaternary volcanic foci (i.e. Cordillera Nevada, Puyehue and Cordón Caulle; Fig. 2), indicating pre-Quaternary existence.

Cembrano and Moreno (1994) interpreted NE-trending domains as hydraulic faults indicating the maximum stress direction (σ_1) prevailing during the Quaternary (Fig 1b). The systematic occurrence of felsic volcanism along NW-trending domains, particularly at Cordón Caulle, and mafic volcanism along NE-trending domains, suggested to Cembrano and Moreno (1994) that NW-oriented domains were compressional in nature, thereby favoring long-term intra-crust residence of magmas and their differentiation, in comparison with extensional NE-domains favoring rapid ascent of magmas.

3. Geology and thermal manifestations of Cordón Caulle

The Cordón Caulle geothermal area (Moreno, 1977) is a NW-SE elongate, 13 km long, 6 km wide flat-topped volcano-tectonic depression hosting the largest active geothermal system of the SVZ (south of 39°S), and a series of monogenetic volcanic centers, including pumice cones, lava-domes and fissure vents. Cordón Caulle spans the largest compositional range of the SVZ (48–72% SiO_2; Gerlach et al., 1988). Volcanism started in the Late-Pleistocene with dominantly mafic effusions, which are exposed along steep glacial valleys all around the depression, and expressed ultimately in post-glacial and historic eruptions of dacite–rhyolite composition, whose deposits (lavas and tephra) blanket the whole area of the depression. Along the southwestern border of the plateau, the so-called Cordón Caulle Fissure (Moreno, 1977), historic fissure eruptions occurred in the years 1921–1922 and 1960. The latter eruption started two days after the Great 1960 Chilean Earthquake (e.g. Cifuentes, 1989), with a former, subplinian phase (Lara et al., 2004) that gave rise to several pumice cones, among which is El Azufral (Fig. 5), where fumaroles and solfatara occur at present (Fig. 5).

Most of thermal manifestations and volcanic centers of Cordón Caulle align parallel to the NW-trending borders of the depression (Fig. 2). Fumaroles, solfatara and acid-sulfate alteration are particularly well developed along the northeastern border, in the areas of Las Sopas and Los Venados (Fig. 5). Along this border, minor steaming-ground areas are also found (e.g. Morro-solfataras; Fig. 5). Hot springs of low flow rate (<10 l/s) are found in the areas of Los Baños and Los Venados (Fig. 5) in association with local steam-heated perched aquifers (Sepúlveda et al., 2004a).

At the southeastern tip of Cordón Caulle is the Puyehue stratovolcano (2236 m; Fig. 2), the bulk of which is made up of numerous basaltic lavas dating back to 0.24 Ma (Harper et al., 2004). An explosive stage spanned between 34 to 2.7 ka (Harper et al., 2004), resulting in extensive pumice deposits and the current morphology of the volcano with a 2.5 km wide caldera. This explosive stage was followed by more effusive andesite and dacite flank eruptions. At present, steaming ground is observed on the northwestern flank of the Puyehue volcano (~2000 m).

Northwest of Cordón Caulle is the ~10 km wide Caldera of Cordillera Nevada (Fig. 2), which represents the remnant of a collapsed stratovolcano with pre-caldera sequences about 1 Ma old (Campos et al., 1998; Lara et al., 2001). Welded ignimbrite deposits

found 15 km to the northeast of the caldera suggests collapse of Cordillera Nevada to be related to an ignimbrite-forming eruption. Cordillera Nevada hosts the main outflow of the geothermal system at the locality of Trahuilco (Fig. 5). About 100 l/s are discharged from vigorous boiling springs with intermittent geyser eruptions up to 5 m high. Most thermal vents correspond to circular, steep-sided craters made up of silica sinter, some of which also display concentric breccia aprons, pointing to episodic hydrothermal eruptions. Permeability is attributed to caldera-related collapse structures, and locally, to sub-parallel jointing (up to ~100 fractures/m) of lavas cropping out nearby.

The basement of Cordón Caulle can be inferred from rock exposures found adjacent to the depression. Late-Miocene intrusions (39–41°S) crop out to the east of the LOFZ, forming part of a regional-scale uplifted block (Lavenu and Cembrano, 1999), as well as locally along the LOFZ main trend. Plutonic fragments contained in strombolian deposits, south of the Puyehue Volcano, together with plutonic inclusion-bearing basaltic bombs of the northern Carrán-Los Venados group (Fig. 2), and prominent plutonic outcrops in the area of Lake Puyehue, give insight into the existence of deep intrusions throughout the Cordón Caulle area. Further north, along the southern shore of the Lake Ranco (Fig. 2), the pre-volcanic basement is more heterogeneous, including Paleozoic sediments and intrusions and Tertiary volcano-clastic sequences (Aguirre and Levi, 1964; Munizaga et al., 1988), which are unconformably overlain by glaciated lavas of the Cordillera Nevada.

4. Methods

4.1. Gravity

4.1.1. Gravity data acquisition and processing

In early 2003, we conducted a gravity survey at Cordón Caulle aimed at delineating the thickness of the uppermost package of dacite–rhyolite lavas and pumice deposits nested in the central depression. Three nearly N45°E-trending profiles averaging 6.5 km in length, with 500–1000 m spacing between consecutive stations, were carried out across the NW-trending depression of Cordón Caulle. The relative gravity measurements were performed with an automated Scintrex CG-3M gravimeter with a micro-Gal (10^{-8} m/s^2) resolution (instrument #9408267 belonging to IRD). Earth tide correction was obtained by use of a Longman (1959) algorithm. The instrumental drift was derived from readings at a remote gravity base station, assuming a linear variation with time. The instrumental drift averaged 0.08 mGal and never exceeded 0.1 mGal for a closure time <7 h. Surveying was done by helicopter to cope with field access difficulties and to reduce time closure for the gravity profiles. The absolute gravity value of our reference base station, was obtained by performing relative gravity measurements at the IGSN71 station 93OSOR (g=980251.06 mGal; Araneda et al., 1999), located 65 to the west of Cordón Caulle.

4.1.2. GPS data acquisition and processing

Stations coordinates and elevation were retrieved by means of differential GPS measurements using Ashtech mono-frequency receivers. Time for data acquisition was set up at 20 min (with a frequency rate of 5 s) in order to achieve point positioning within a few decimeters accuracy. The base reference station was located at the center of the surveyed area to ensure baseline length between rover and base receivers no greater than 6 km.

The coordinates of the base station were transformed to the International Terrestrial Reference Frame system (ITRF2000) using data from neighboring permanent stations of the IGS (International GPS Service) global GPS network. Station coordinates were computed with Ashtech Solution 2.6 Software. The final accuracy of the gravity site positions with respect to the base station is estimated to be better than 5 cm and 10 cm for horizontal and vertical components, respectively, fitting the requirements of this gravity survey.

4.1.3. Computation of gravity anomalies

Theoretical gravity was calculated using the 1980 formula (Torge, 1989):

$$g_t = g_{ec}\left(1 + C_1\sin^2\varphi + C_2\sin^2 2\varphi\right) \quad (1) \qquad (1)$$

where g_t=theoretical gravity; g_{ec}=978032.7 mGal (normal gravity at Equator), C_1=0.0053024, C_2=−0.0000058 and φ=latitude [radians].

Free-Air ($\Delta g_{\text{free-air}}$) and Bouguer ($\Delta g_{\text{b}}$) reductions were obtained as follows:

$$\Delta g_{\text{free-air}} = 0.3086h \quad (2)$$

$$\Delta g_{\text{b}} = 2\pi G\rho h = 0.1119h \quad (3)$$

where h, G, and ρ are height (in meters), Universal Gravity Constant, and density (2670 kg/m^3; average crustal density), respectively. We also computed a local and regional terrain correction (Δg_{topo}) using the Xcceleration Gravity module of Oasis Montaj Software (Geosoft version 5.15). Local and regional Digital Elevation Models (DEM) were obtained from the newly available global topography database (90 m standard resolution) acquired by the Space Radar Topography Mission (SRTM, NASA) and freely distributed by USGS (ftp://edcsgs9.cr.usgs.gov/pub/data/srtm/South_America/). Depending on the station location, the amplitude of the terrain correction on the surveyed area ranged between 5 and 15 mGal. The final Bouguer anomaly (BA) was calculated as follows:

$$\text{BA} = g_{\text{obs}} - g_{\text{t}} - \Delta g_{\text{b}} + \Delta g_{\text{free-air}} + \Delta g_{\text{topo}} \quad (4)$$

The Bouguer anomalies of Cordón Caulle are listed in Table 1. The interpolated Bouguer anomalies are shown in Fig. 3. For gravity modeling, a residual anomaly (RA) was calculated at Cordón Caulle, by

Table 1
Bouguer anomalies of Cordón Caulle measured along three NE-trending profiles

Estation	UTM (m)		Elevation (m)	Gravity (mGal)		Correction (mGal)			Anomaly (mGal)	
	N	E		Observed	Theoretical	Free-air	Bouguer	Terrain	Bouguer	Residual
Profile 1										
101	5505800.0	738269.9	1460.7	979883.2	980220.2	450.8	163.5	5.4	−44.3	−1
102	5506760.1	738947.4	1471.5	979874.6	980219.5	454.1	164.7	4.4	−51.0	−8
103	5508070.3	739814.7	1682.6	979813.8	980218.4	519.2	188.3	7.6	−65.9	−22
104	5508527.0	740295.2	1547.7	979845.4	980218.0	477.6	173.2	4.9	−63.3	−19
105	5509067.0	740820.3	1438.6	979868.5	980217.6	444.0	161.0	4.3	−61.7	−17
106	5509699.6	741531.3	1486.0	979859.7	980217.0	458.6	166.3	4.4	−60.6	−16
107	5510003.8	741975.0	1466.3	979864.6	980216.8	452.5	164.1	4.9	−58.8	−14
Profile 2										
201	5509279.4	735845.1	1463.2	979876.5	980217.5	451.5	163.7	6.1	−47.0	−2
202	5509950.6	736307.2	1570.8	979848.0	980217.0	484.7	175.8	6.6	−53.4	−8
203	5510601.3	736471.0	1746.0	979800.9	980216.4	538.8	195.4	10.7	−61.3	−16
204	5511313.5	737302.5	1541.2	979847.0	980215.8	475.6	172.5	5.1	−60.5	−14
205	5511885.8	737904.0	1516.7	979850.7	980215.4	468.1	169.7	4.5	−61.7	−15
206	5512265.1	738383.0	1512.8	979851.7	980215.0	466.8	169.3	4.4	−61.4	−14
207	5513280.3	739354.2	1609.9	979829.9	980214.2	496.8	180.1	6.2	−61.4	−14
208	5514071.1	740200.2	1612.3	979833.3	980213.5	497.5	180.4	9.7	−53.4	−5
Profile 3										
301	5511299.2	732782.6	1714.7	979813.8	980216.0	529.1	191.9	16.2	−48.6	−4
302	5511865.2	733546.4	1702.7	979817.4	980215.5	525.4	190.5	11.2	−51.9	−6
303	5512555.8	733950.1	1572.5	979846.1	980214.9	485.3	176.0	6.2	−53.2	−8
304	5513054.4	734375.7	1616.2	979832.3	980214.5	498.8	180.8	6.4	−57.8	−12
305	5514099.1	735002.5	1604.7	979830.2	980213.7	495.2	179.6	6.6	−61.1	−15
306	5514655.3	735238.4	1594.1	979830.3	980213.2	491.9	178.4	7.0	−62.3	−16
307	5515407.9	736000.0	1465.9	979857.9	980212.6	452.4	164.0	5.8	−60.5	−14
308	5515871.2	736480.0	1703.4	979800.9	980212.2	525.7	190.6	13.3	−62.8	−16
309	5516628.7	737021.2	1504.2	979857.8	980211.6	464.2	168.3	6.8	−51.1	−4
310	5517323.5	737169.1	1731.4	979801.4	980211.0	534.3	193.7	15.9	−53.1	−6
311	5517700.3	737572.6	1637.7	979826.4	980210.7	505.4	183.3	13.8	−48.3	−1

Elevation is referenced to the WGS94 datum (1 mGal=10^{-5} m/s^2 =10 μN/kg).

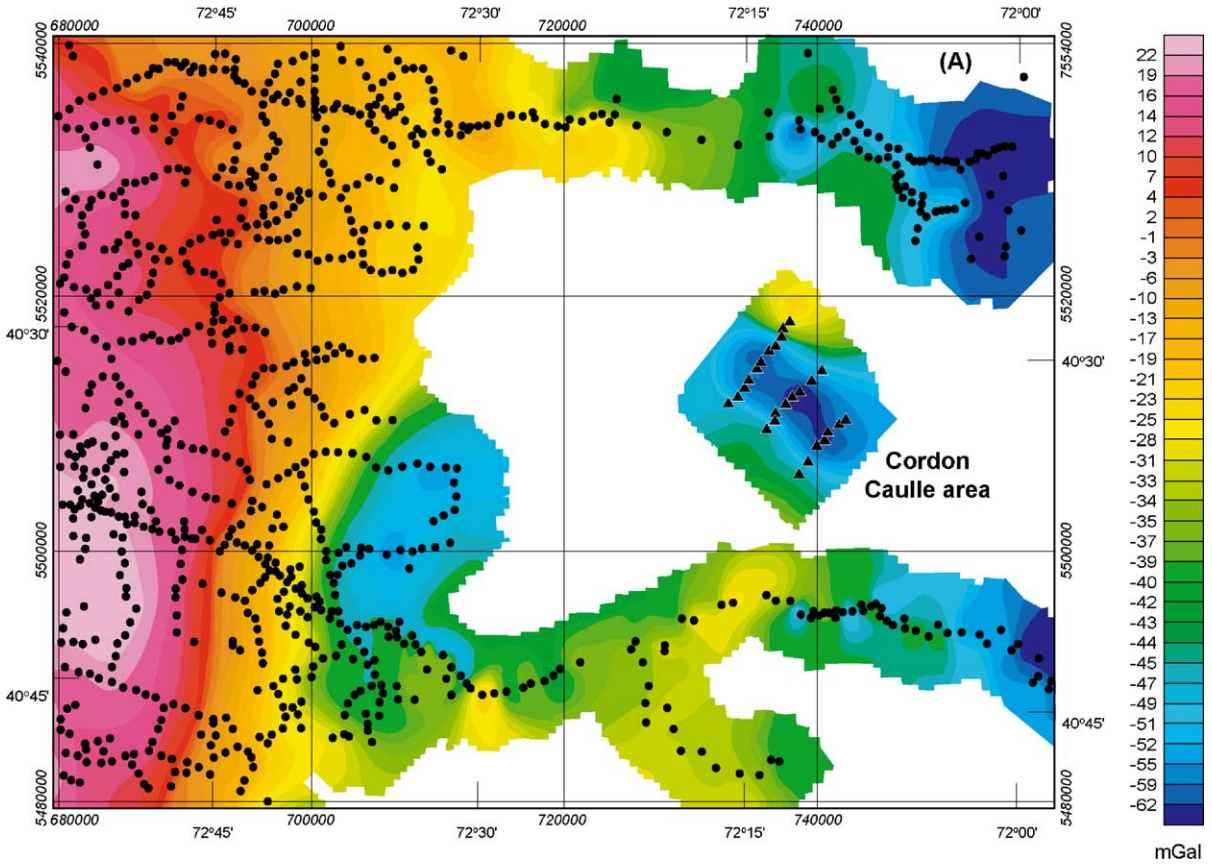

Fig. 3. Interpolation of the Bouguer anomalies of Cordón Caulle. Regional data from Araneda et al. (1999).

removing the long wavelength component of the regional gravity field. RA was calculated as:

$$RA = BA_{obs} - BA_{reg} \quad (5)$$

where BA_{obs} is the observed (local) Bouguer anomaly (Profile 2; Table 1), and BA_{reg} is the interpolated regional Bouguer anomaly by first-order polynomial fitting. Regional Bouguer anomalies were taken from (Araneda et al., 1999). A representative regional gravity gradient for the surveyed area was obtained by interpolating two east-west transects lying both north and south of Cordón Caulle (UTM 720000-760000 E; Fig. 4). The so-obtained gravity gradient is about −0.8 mGal/km and accounts for a well-defined west-to-east decrease of the Bouguer anomalies (Fig. 3).

In order to better constrain density ranges to be used in gravity modeling and interpretation, density measurements were performed in basalts (including samples LICAN, PUYEHUE, ICULPE and NEVADA) and granitoids (sample INT), averaging 2654 ± 26 kg/m^3 ($n = 9$). For simplicity, a background density

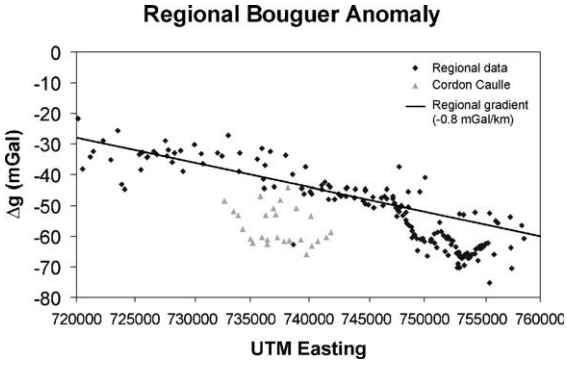

Fig. 4. (A) Representative first-order polynomial fitting of the Regional Bouguer anomaly at the surveyed area.

of 2650 kg/m^3 was adopted. Measured densities in dacite–rhyolite lavas (CCIV unit in nomenclature of Moreno, 1977) averaged 2370 ± 130 kg/m^3 (n = 3). Pumice fragments collected from surface deposits had much lower density (often <1000 kg/m^3). In order to incorporate the effect of compaction with depth in pumice deposits, an average density of 1700 kg/m^3 was assumed for gravity modeling.

4.2. Ar–Ar dating and Al-in hornblende geobarometry

Whole-rock and biotite step-heating ^{40}Ar–^{39}Ar gas release determinations were conducted at the National Geological Survey, Chile (SERNAGEOMIN) to constrain the timing of volcanic activity and the cooling history of crystalline basement rocks. Age determinations combined with geobarometry were used to estimate exhumation rates. Whole-rock dating was performed in porphyritic basalt/basaltic-andesite lavas (52–55 wt.% SiO_2; K_2O within 0.75–1.15 wt.%). Sample NEVADA was recovered from the top of the northwestern wall of the caldera of Cordillera Nevada (1530 m), representing one of the latest eruptive events prior to the collapse of Cordillera Nevada. Sample LICAN comes from the bottom of a glacial-fluvial valley, and together with sample PUYEHUE, which comes from the base of a 500 m high glacial scarp along the northwestern shore of Lake Puyehue, is intended to constrain the age of the oldest exposed stratigraphic levels. In all these locations, monotonous sequences of basalt interbedded with lahars were observed. Biotite grains were recovered from an unaltered granodiorite intrusion (sample INT; Fig. 2) cropping out to the east of Cordón Caulle, along the LOFZ main trend.

Neutron-irradiation was performed at the nuclear reactor of the National Commission of Nuclear Energy (CChEN). All samples were wrapped in cadmium foil and placed in discs of pure aluminum together with a neutron fluence-monitor (Fish Canyon Sanidine Standard; age = 28.03 ± 0.18 Ma; Renne et al., 1994). Prior to irradiation of whole-rock samples, plagioclase fenocrysts were separated in order to minimize the effect of Ca on ^{39}Ar production. For isotopic determination, samples were fused using a CO_2-laser system operating at a nominal output power of 30 W, and then analyzed in a MAP 215-50 mass spectrometer. Reported Ca/K ratios (Table 2) were calculated using ^{37}Ar/^{39}Ar ratios. Analytical conditions of the Ar–Ar system are described in more detail by Pérez de Arce et al. (2000, 2003).

Chemical analysis in hornblende from sample INT were obtained using an electron microprobe CAMEBAX SU-30 at the University of Chile. All the elements were analyzed using X-Ray wavelength scattering spectrometry (WDS), with pure standards certified by P and H Developments. Quantitative analysis was performed by a CAMECA SX-50 Software. The total aluminum (Al^{tot}) per formula was calculated according to the method of Leake et al. (1997), which also allows estimation of the proportion of Fe^{3+} in hornblende.

The Al-in-hornblende geobarometer was first empirically formulated (Hammarstrom and Zen, 1986; Hollister et al.,1987) and then experimentally calibrated for the near H_2O-saturated solidus assemblage quartz + alkali feldspar + plagioclase + hornblende biotite + Fe–Ti oxide, for oxygen fugacities (fO_2) bracketed between the nickel–nickel oxide (NNO) and hematite–magnetite (HM) buffers (Johnson and Rutherford, 1989; Schmidt, 1992), and for temperatures and pressures of 655–700 °C and 2.5–13 kbar (1 kbar = 100 MPa), respectively. Errors in pressure estimates progressively reduced from ±1–3 kbar (Hammarstrom and Zen, 1986; Hollister et al., 1987) to ±0.6 kbar (Schmidt, 1992), allowing application to shallow intrusions.

Formulations of Schmidt (1992, Eq. (6)) and Anderson and Smith (1995; Eq. (7)) were adopted for this study:

$$P_1(\pm 0.6\ \text{kbar}) = 4.76\text{Al}^{\text{tot}} - 3.01 \tag{6}$$

$$\begin{aligned} P_2(\pm 0.6\ \text{kbar}) = {} & 4.76\text{Al}^{\text{tot}} - 3.01 \\ & - \{[T(^\circ\text{C}) - 675]/85\} \\ & \times \{0.530\text{Al}^{\text{tot}} + 0.005294 \\ & \times [T(^\circ\text{C}) - 675]\} \end{aligned} \tag{7}$$

Anderson and Smith's (1995) barometer is a revised version of the Schmidt's barometer, which incorporates the effect of the temperature in Al^{tot}. The Ti-in-horblende geothermometer proposed by Otten (1984) allows independent assessment of temperature, provided that enough Ti is available (i.e.

Table 2
Analytical $^{40}Ar/^{39}Ar$ results in volcanic (whole rock) and crystalline (biotite) basement rocks of the Cordón Caulle geothermal region

Step no.	Ca/K	^{39}Ar (%)	$^{40}Ar/^{39}Ar_K$	Aparent age (Ma)	$\pm\sigma$	$^{36}Ar/^{40}Ar$ isocr	±%	$^{39}A/^{40}Ar$ isocr	±%
NEVADA whole rock (J= 0.0011963 ± 0.0000076)									
1	1.67	21.3	0.0977	0.211	0.021	0.003162	0.7	0.67292	0.27
2	2.69	19.4	0.0919	0.199	0.021	0.003029	1.2	1.14336	0.33
3	4.55	15.9	0.1117	0.242	0.024	0.003016	1.2	0.97388	0.29
4	6.90	10.6	0.0938	0.203	0.041	0.003154	1.5	0.72636	0.24
5	8.79	6.5	0.1452	0.314	0.061	0.003100	1.8	0.57821	0.45
6	10.47	10.1	0.1459	0.316	0.051	0.003187	1.0	0.39919	0.29
7	10.51	9.7	0.2722	0.589	0.092	0.003200	0.9	0.19957	0.35
8	26.56	6.6	0.3133	0.678	0.145	0.003217	1.1	0.15812	0.27
				Integrated age		Isochron age			
				0.300	0.030	0.117 ± 0.015			
PUYEHUE whole rock (J= 0.0010169 ± 0.0000051)									
1	2.53	0.3	−1.3822	−2.544	1.569				
2	3.19	5.4	−0.6969	−1.282	0.129				
3	3.85	16.6	0.0744	0.137	0.034				
4	3.75	22.0	0.1674	0.308	0.019				
5	3.59	24.2	0.1539	0.283	0.020				
6	4.17	14.9	0.2008	0.369	0.028				
7	8.23	10.6	0.2412	0.444	0.066				
8	13.34	6.0	0.0398	0.073	0.087				
				Integrated age					
				0.190	0.030				
ICULPE whole rock (J= 0.0010539 ± 0.0000053)									
1	1.17	0.8	0.8034	1.530	0.578				
2	1.15	20.5	0.0967	0.184	0.047				
3	1.64	26.1	0.0492	0.094	0.030				
4	2.72	25.5	0.0507	0.097	0.029				
5	4.43	17.7	0.0648	0.124	0.038				
6	6.45	9.4	0.0945	0.180	0.068				
				Integrated age					
				0.140	0.040				
LICAN whole rock (J= 0.0010321 ± 0.0000052)									
1	1.14	0.4	−0.374	−0.698	0.871				
2	2.92	11.1	0.178	0.332	0.062				
3	3.64	21.0	0.080	0.149	0.030				
4	4.23	19.0	0.122	0.227	0.032				
5	4.82	14.2	0.042	0.079	0.033				
6	5.03	10.2	−0.017	−0.032	0.053				
7	5.91	14.9	0.140	0.261	0.048				
8	9.85	9.2	0.153	0.286	0.068				
				Integrated age					
				0.180	0.030				
INT biotite (J= 0.001291 ± 0.000004)									
1		0.2	0.3081	−0.72	1.89				
2		3.4	1.4180	3.31	0.24				
3		10.8	2.3590	5.50	0.06				
4		11.1	2.3417	5.46	0.04				
5		9.0	2.3176	5.40	0.04				
6		8.6	2.3192	5.41	0.04				

Table 2 (*continued*)

Step no.	Ca/K	^{39}Ar (%)	^{40}Ar/^{39}Ar$_K$	Aparent age (Ma)	$\pm\sigma$	^{36}Ar/^{40}Ar isocr	$\pm$%	^{39}A/^{40}Ar isocr	$\pm$%
INT biotite (J= 0.001291 ± 0.000004)									
7		11.8	2.3612	5.05	0.04				
8		13.5	2.3267	5.42	0.03				
9		16.2	2.3232	5.42	0.02				
10		10.3	2.3464	5.47	0.03				
11		5.0	2.3549	5.49	0.04				
				Integrated age					
				5.36	0.05				

Ti-bearing phases must be present) and that oxygen fugacity is near the QFM buffer:

$$T(^{\circ}\mathrm{C}) = 1204Ti + 545 \quad (T<970^{\circ}\mathrm{C}) \tag{8}$$

where Ti is the number of cations per formula on the basis of 23 oxygens.

Sample INT is characterized by quartz, plagioclase, K-feldspar, biotite, hornblende, magnetite and titanite and minor mafic inclusions. The required assemblage was therefore present. Hornblende rims coexisting with quartz were selected for measurements, in order to ensure near-solidus crystallization,

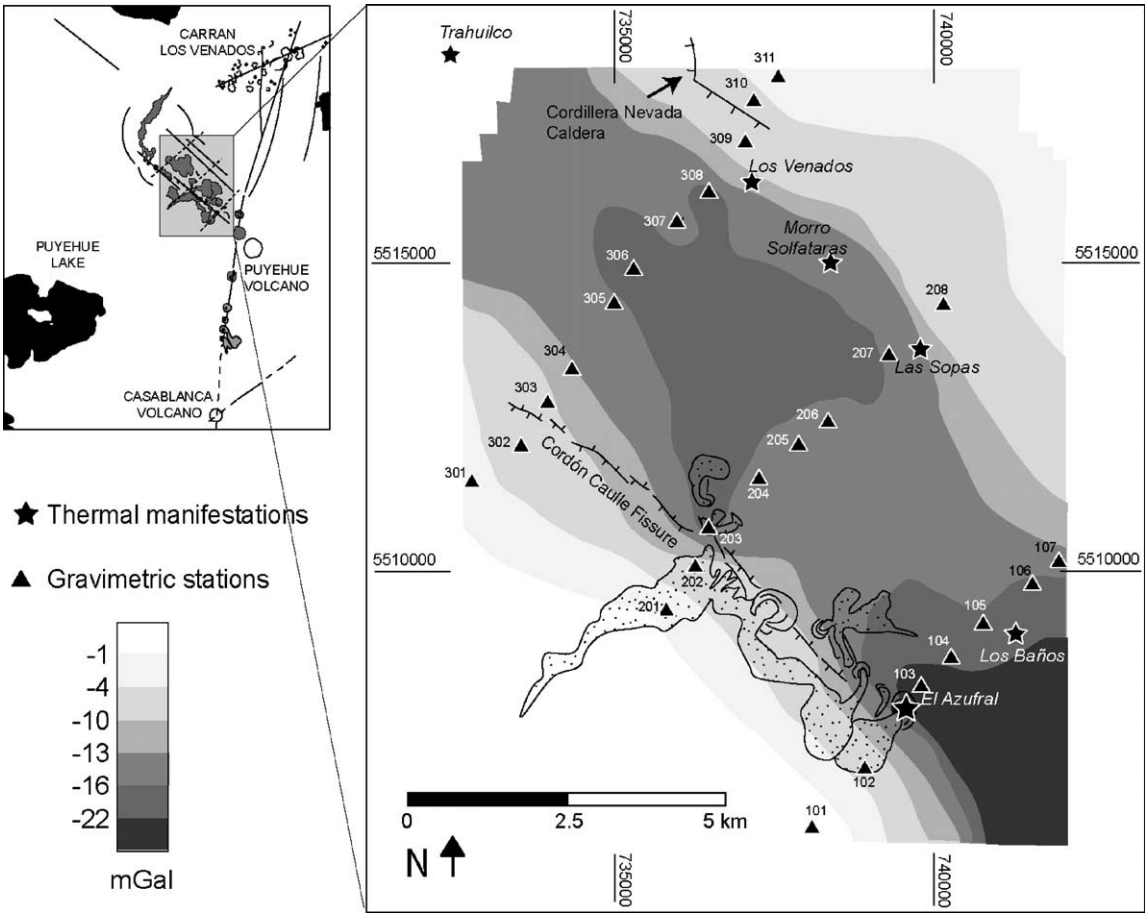

Fig. 5. Interpolated residual anomaly of Cordón Caulle. Lava flows of the 1960 eruption are also shown.

and minimize the likelihood of Al-exchange with plagioclase, as dictated by the reaction 2 quartz+2 anortite=orthoclase+Tschermak. Ideal fO_2 conditions (within calibration range) were tested against two criteria: $R=Fe^{3+}/(Fe^{3+}+Fe^{2+})>2$, and Fe/(Fe+Mg) within 0.40–0.65 (e.g. Blundy and Holland, 1990).

The following expression was used in the conversion of pressure to depth of emplacement (z):

$$P(\pm 0.4\ \text{kbar}) = \rho g z = 2670\left(\text{kg/m}^3\right) \times 9.8\left(\text{m/s}^2\right) \times z(\text{km}) = 0.26z \quad (9)$$

5. Results

5.1. Gravity

The three gravity profiles of Cordón Caulle consistently show a decrease in the residual anomalies Bouguer anomalies from a maximum between −45 and −50 mGals, along the borders of the depression, towards a minimum between −60 to −65 mGals, in the central part of the depression (Table 1; Fig. 3). The residual anomaly, as presently calculated (Eq. (5); Table 1), reaches a maximum amplitude of about −20 mGal at the center of the depression. Since the three profiles reproduced a similar U-shaped residual anomaly curve (Fig. 5), we selected the central profile (i.e. profile 2; Table 1) for gravity modeling, using a 2D approach. For 2D-modeling, we used GRV-2D Win software which is based on the approach of Talwani et al. (1959). In accordance with the relatively short wavelength of the residual anomaly, on the order of 5 km (measured parallel to the direction of the profiles; Fig. 6), we assumed the presence of a shallow anomalous body (depth <5 km) to model the residual anomaly. Based on our geological interpretations pointing to a shallow infill of felsic lavas and tephra overlying a basement of more dense basaltic lavas and crystalline basement rocks (with an average density of 2650 kg/m^3) at Cordón Caulle, we adopted a density contrast of −650 kg/m^3 for the shallow body, whose inferred geometry is shown in Fig. 6. The average thickness of the shallow body that matched the residual anomaly was 620 m (Fig. 6). In a second model, we added a hypothetical low-density "hydrothermal" body representing hydrothermally fractured zones at 950–1450 m depth (Fig. 7). By assuming 10–15% porosity (Φ) and a reservoir temperature of 250 °C (Sepúlveda et al., 2004b), a

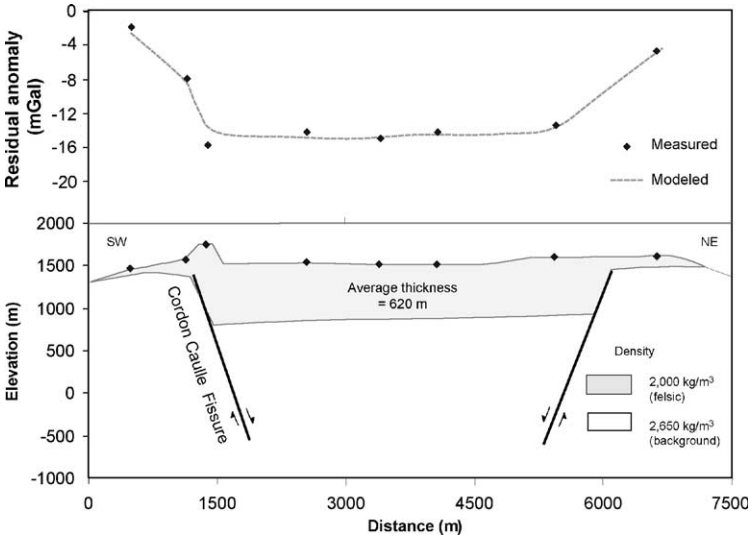

Fig. 6. 2D-gravity model of the residual anomaly of Cordón Caulle, using data from Profile 2 (Table 1), with a selected density contrast of −650 kg/m^3 for a 620 m thick body. The edges of the depression are interpreted as normal faults.

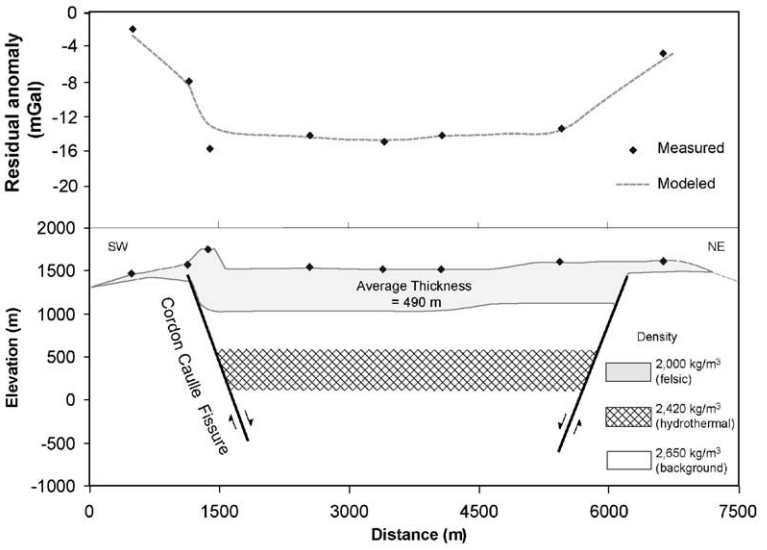

Fig. 7. 2D-gravity model of the residual anomaly of Cordón Caulle, using data from Profile 2 (Table 1), adding (with respect to Fig. 6) a second anomalous body representing deep hydrothermally induced porosity.

saturated density (ρ_s) was estimated for this hydrothermal body as:

$$\rho_s = (1 - \Phi)\rho_r + \Phi\rho_w \quad (10)$$

where ρ_w is the density of water at reservoir temperature (800 kg/m^3) and ρ_r is the background rock density (2650 kg/m^3), yielding ρ_s=2420 kg/m^3 (i.e. density contrast of −230 kg/m^3). In this scenario, the average thickness of the shallow infill that matched the residual anomaly was 490 m (Fig. 7).

5.2. Ar–Ar dating and Al-in-hornblende barometry

Analytical $^{40}Ar/^{39}Ar$ results are listed in Table 2. $^{40}Ar/^{39}Ar$ release spectra and mean plateau ages are given in Figs. 8 and 9. Mean ages are provided with 2σ errors, including the uncertainty in the parameter J (Pérez de Arce et al., 2003). Sample PUYEHUE yielded the oldest age of volcanic rocks (0.31 ± 0.03 Ma; Fig. 9). Two runs were performed in NEVADA; the first one (NEVADA1; Fig. 8), which did not yield any plateau age, showed a first step with a high apparent age, pointing to excess Ar. The spectra of the second run (NEVADA2; Fig. 9) did yield a plateau age (0.22 ± 0.04 Ma; Fig. 9). Both spectra showed an increasing progression in the apparent ages towards higher temperatures, correlated with increasing Ca/K ratios (Table 2), suggesting release of excess Ar from pyroxens. The combined inverse isochron ($^{39}Ar/^{40}Ar$ vs. $^{36}Ar/^{40}Ar$) obtained from these two runs (not shown) yielded an age of 0.117 ± 0.015 Ma (initial $^{40}Ar/^{36}Ar$ intercept of 309.0 ± 1.8, MSWD=1.5). The inverse isochron age of NEVADA2 is 0.130 ± 0.020 Ma (Fig. 10). Since excess Ar appeared to be present, we used the inverse isochron age of NEVADA2 to constrain the time for the collapse of Cordillera Nevada (i.e. younger than approximately 0.13 Ma). Note that

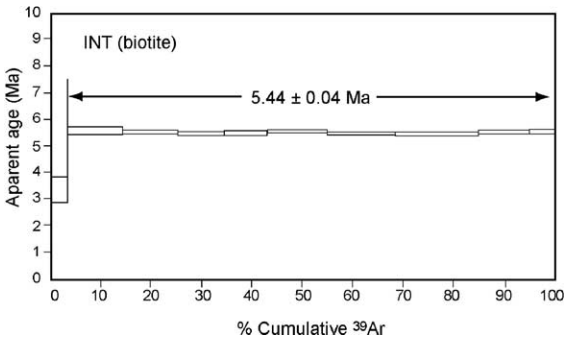

Fig. 8. Biotite ^{40}Ar–^{39}Ar release spectra and mean plateau age obtained for sample INT (±2σ).

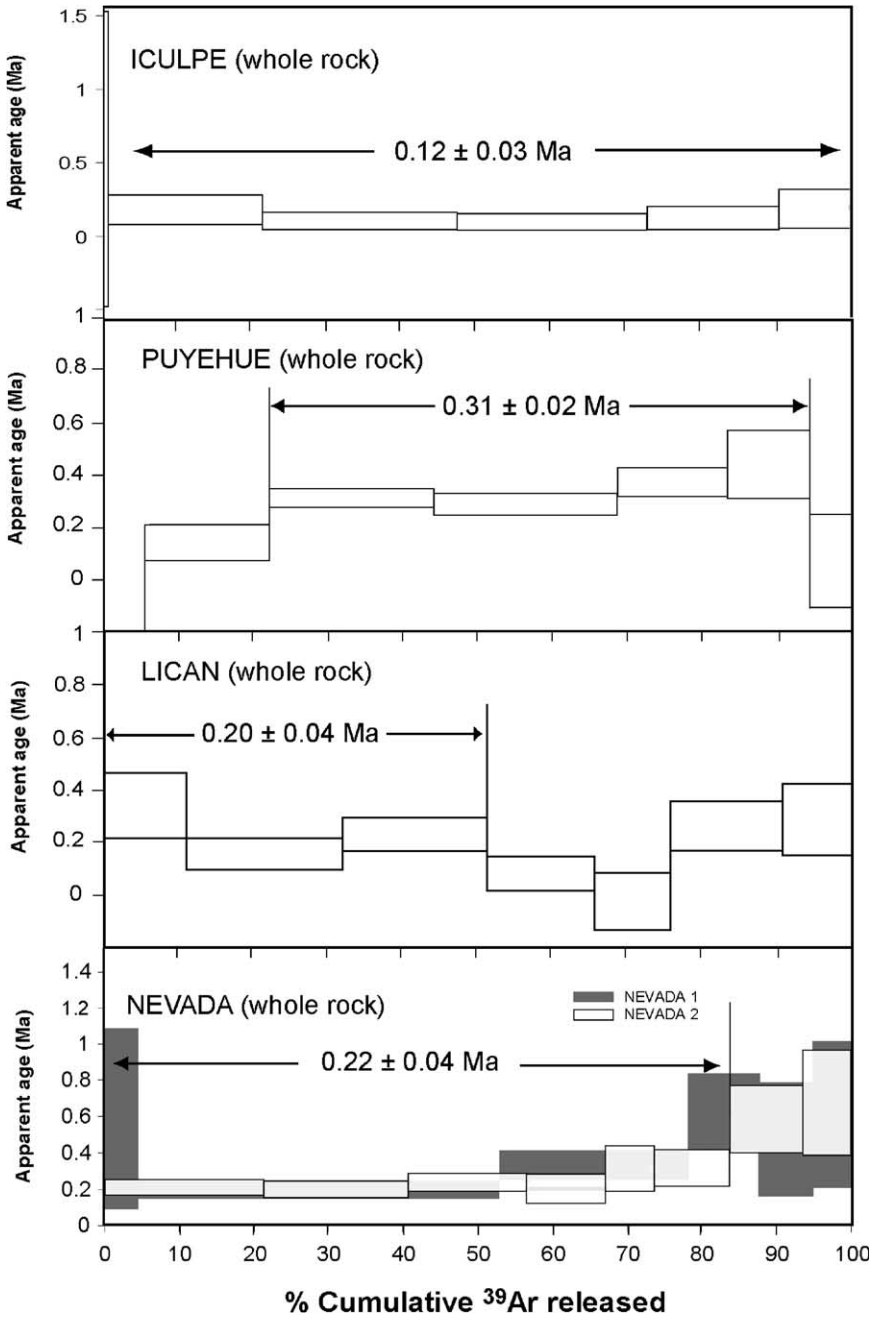

Fig. 9. Whole rock ^{40}Ar–^{39}Ar release spectra and mean plateau ages obtained for volcanic rocks ($\pm 2\sigma$).

ICULPE, whose provenance is linked to Cordillera Nevada, yielded an age of 0.12 ± 0.03 Ma (Fig. 9) which is concordant with the isochron age of NEVADA2.

Representative microprobe analysis of hornblende rims are listed in Table 3. Pressures estimated by Eqs. (6) and (7) are $P_1 = 1.9 \pm 0.2$ kbar ($n = 6$) and $P_2 = 1.6 \pm 0.2$ kbar ($n = 5$), respectively, equivalent to

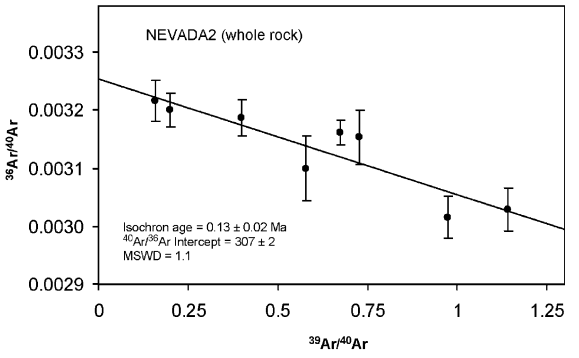

Fig. 10. Inverse isochron age obtained for NEVADA2.

depths of emplacement (z) between 7.3 and 6.2 km (Eq. (9)). z values in combination with the Ar–Ar age of 5.44 ± 0.04 Ma of sample INT (Fig. 8), which is similar to other radiometric ages in the region (e.g. U-Pb: 5.3 ± 0.8 Ma at ~40° 10'S; Campos et al., 1998), lead to an exhumation rate (v) between 1.10 and 1.34 mm/year. Both a linear variation of v with time and a slow exhumation (or rapid cooling) between ~700° (crystallization temperature for hornblende; Eq. (8)) and ~350 °C (closure temperature of biotite to Ar) were assumed for calculation. Ti-in-hornblende temperatures used in the calculation of P_2 did not include run INT27, which turned out to largely increase the scattering of Ti data (final range Ti = 0.15 ± 0.04). Ti-in-hornblende temperatures averaged 710 °C (range 680–747 °C; Eq. (8)), which is 60 °C above the H_2O-saturated solidus temperature (650 °C; Anderson and Smith, 1995). Although oxidation conditions near the NNO buffer, inferred from the presence of quartz and magnetite in the absence of fayalite (R = 0.12; Spear, 1981), Fe/(Fe + Mg) = 0.37 and R = 0.2 (Table 3), limit the use of the Ti-in-hornblende geothermometer, they are adequate for the Schmidt's (1992) barometer.

6. Discussion

6.1. Cordón Caulle: a NW-trending domain

The presence of a long-lived NW-trending crustal anisotropy at Cordón Caulle (e.g. Cembrano and Moreno, 1994; López-Escobar et al., 1995) gives strong insight into the existence of an ancestral fissure system underlying the current depression of Cordón Caulle. We use the age of PUYEHUE (approximately 0.3 Ma; Fig. 9) as a proxy for the onset of volcanism associated with the ancestral Cordón Caulle. Based on the $^{49}Ar/^{39}Ar$ age of NEVADA (Fig. 10), we suggest that between approximately 0.3–0.1 Ma, both the ancestral Cordón Caulle and Cordillera Nevada remained active volcanic centers.

Volumes emitted by the Puyehue Volcano and Cordón Caulle were estimated as $\sum(\text{area}_i \times \text{thickness}_i)$, using a 1 km × 1 km resolution grid superimposed on topography (Fig. 11), where $\sum\text{area}_i$ delimits the total extension of the volcanic products associated with a volcanic center. Irrespective of the resolution of the grid, precise volume estimations for a particular volcanic center are hampered by uncertainties inherent to thickness estimations. Thickness depends upon topographic height and usually unconstrained depth of basement. In the case of Cordón Caulle, further uncertainty in thickness estimation arises from the poorly constrained degree of interfingering with the adjacent Cordillera Nevada. Within the area of the depression of Cordón Caulle, we fixed depth of basement at 500 m to account for interfingering of Cordillera Nevada and pre-volcanic intrusions. Outside the depression of Cordón Caulle, where similar contact relationships can be invoked, volumes were calculated as $1/2\ \sum(\text{area}_i \times \text{topographic height}_i)$. At Puyehue volcano, depth of basement was fixed at 300 m. The volume of felsic material of Cordón Caulle is calculated using the thickness of 490 m from our gravity model, and the area of the central depression as shown in Fig. 11. The so-calculated volume is on the order of 33 km^3. For an equal proportion of felsic lavas and pumice, the dense rock equivalent (DRE) volume is:

$$\text{DRE} = 0.5\ \text{volume} + 0.5\ \text{volume} \times \rho_{\text{tephra}}/\rho_{\text{magma}}. \quad (11)$$

Taking ρ_{tephra} = 1700 kg/m^3 and ρ_{magma} = 2300 kg/m^3 leads to a DRE volume of 28 km^3. The estimated DRE volume represents about 20% of the total volume estimated for Cordón Caulle (150 km^3).

Based on our estimations of volume and area and available $^{40}Ar/^{39}Ar$ dating, long-term output rates can be calculated at Puyehue volcano and Cordón Caulle (i.e. km^3/km^2/year). For comparison, output rates are normalized to an area of 30 × 30 km (i.e. 10^3 km^2) and

Table 3
Representative microprobe analysis from hornblende rims from sample INT

Run code	INT14	INT24	INT27	INT28	INT33	INT44
SiO_2	48.58	48.16	49.46	49.23	49.12	49.40
TiO_2	1.00	1.52	1.97	1.50	1.04	1.17
Al_2O_3	5.81	6.38	6.21	6.26	6.01	5.81
FeO	16.70	15.66	12.92	13.96	14.36	14.46
MnO	0.76	0.41	0.35	0.28	0.52	0.54
MgO	12.65	13.61	14.79	14.56	13.91	14.04
CaO	10.50	11.11	11.23	11.17	11.15	11.39
Na_2O	1.37	1.47	1.67	1.53	1.55	1.40
K_2O	0.47	0.32	0.29	0.38	0.47	0.51
Total	97.85	98.64	98.89	98.89	98.12	98.73
Structural formula						
Si	7.120	6.983	7.075	7.061	7.131	7.135
Al^{IV}	0.880	1.017	0.925	0.939	0.869	0.865
Sum T	8.00	8.00	8.00	8.00	8.00	8.00
Al^{IV}	0.122	0.074	0.123	0.119	0.159	0.124
Ti	0.111	0.166	0.212	0.162	0.113	0.127
Fe^{3+}	0.483	0.420	0.267	0.361	0.313	0.303
Mg	2.765	2.943	3.153	3.113	3.010	3.023
Fe^{2+}	1.520	1.396	1.244	1.244	1.404	1.423
Mn	0.000	0.000	0.000	0.000	0.000	0.000
Sum C	5.00	5.00	5.00	5.00	5.00	5.00
Mg	0.000	0.000	0.000	0.000	0.000	0.000
Fe^{2+}	0.045	0.082	0.034	0.069	0.026	0.021
Mn	0.095	0.050	0.043	0.034	0.064	0.066
Ca	1.649	1.726	1.721	1.716	1.734	1.762
Na	0.212	0.141	0.202	0.180	0.176	0.151
Sum B	2.00	2.00	2.00	2.00	2.00	2.00
Na	0.178	0.271	0.261	0.246	0.260	0.242
K	0.088	0.059	0.052	0.070	0.086	0.094
Sum A	0.27	0.33	0.31	0.32	0.35	0.34
Total	15.266	15.331	15.313	15.315	15.347	15.336
P (± 0.6 kbar)						
Schmidt (1992)	1.8	2.2	2.0	2.0	1.9	1.7
Anderson and Smith (1995)	1.5	1.9	1.7	1.7	1.6	1.4
					mean	1.8
T (°C)		1.7	1.4	1.3	1.8	1.5
Ti (23 oxygens basis)	0.112	0.168	0.213	0.163	0.114	0.128
Otten (1984)	680	747	802	742	682	699
*INT27 ruled out					*mean	710
$Fe_{tot}/(Fe_{tot}+Mg)$	0.43	0.39	0.33	0.35	0.37	0.37
$Fe^{3+}/(Fe^{3+}+Fe^{2+})$	0.24	0.22	0.17	0.22	0.18	0.17

Pressure estimates are also given.

a period of 10^4 year. Takada (1994) reported normalized output rates from several volcanoes worldwide showing close correlation between low normalized output rate rates (<10 km^3) and monogenetic volcanism. Examples include the Rhine Graben (0.6 km^3) and Michoacán (0.5 km^3; Fig. 12). He also reported normalized output rates of polygenetic volcanoes, typically ranging from 50 km^3 (e.g. Etna or Fuji) up to 2500 km^3 (e.g. Mauna Loa). The normalized output of Puyehue volcano is 46 km^3, doubling the normalized output of Cordón Caulle (21 km^3; Fig. 11). The confluence of arc-parallel and oblique domains in the area of the Puyehue volcano (Fig. 2) reasonably explains its comparatively higher output rate. The

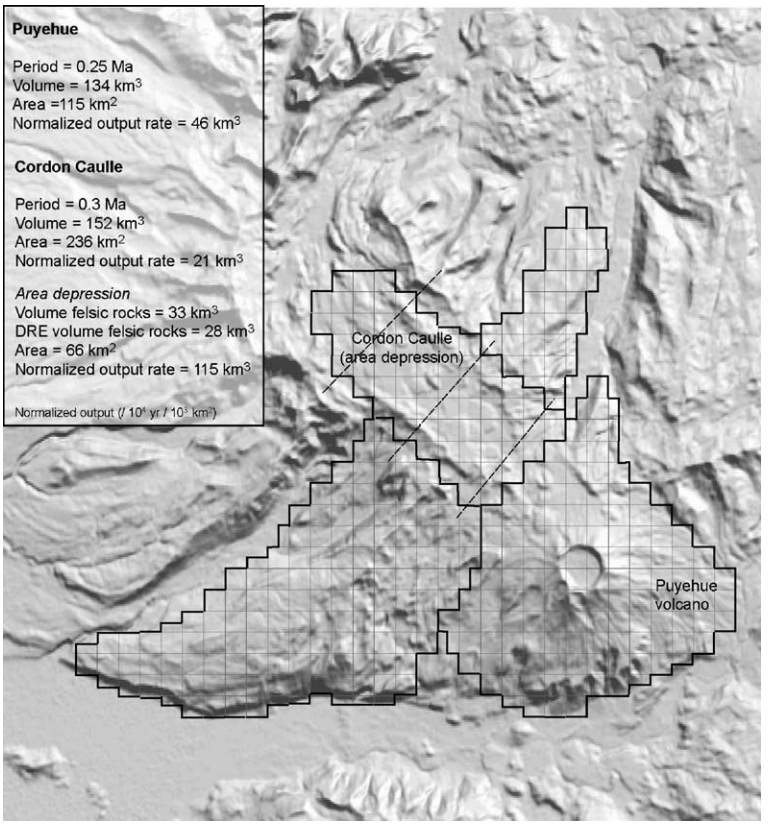

Fig. 11. Erupted volumes and normalized output rates of Puyehue and Cordón Caulle. Volumes are approximated by the summation of 1×1 km blocks over the total area occupied by the products of the volcanic centers, with the thickness of each block delimited by topography (upper limit) and corrected for depth of basement and degree of interfingering with the adjacent volcanic centers (e.g. Cordillera Nevada–Cordón Caulle). Following Takada (1994), long-term normalized output rates are calculated as volume (km^3)/area (km^2)/period (Ma) × normalization area ($=10^3$ km^2) × normalization period ($=10^4$ year). Gravimetric profiles are shown for reference.

higher output of Puyehue relative to Cordón Caulle would be also the primary cause for the contrasting style of volcanism between these two areas (i.e. polygenetic at Puyehue and monogenetic at Cordón Caulle), in the sense of Takada (1994).

The normalized output rate of felsic material at Cordón Caulle is calculated assuming a period of silicic volcanism similar to that of the adjacent Puyehue volcano (34 ka; Harper et al., 2004). This assumption rests on the spatial closeness and geochemical affinity of evolved lavas from Puyehue and Cordón Caulle, suggesting a common source and evolution (Gerlach et al., 1988). Normalized output rates of felsic material calculated in this way are about 120 km^3, which is typical for polygenetic centers but uncommon for monogenetic fields. Takada (1994) formulated a crack coalescence theory according to which the likelihood of having a monogenetic center decreases in favor of a polygenetic cone with increasing output rate, unless differential stress increases. Under high differential stress, the crack coalescence theory predicts that dikes would propagate upward isolate forming a monogenetic center at surface, for a wide range of output rates (Fig. 13). Following Takada (1994), high output rates of silicic volcanism at Cordón Caulle are most likely to have been accompanied by a high differential stress in order to permit monogenetic volcanism. By assuming that propagation of dikes is favorable along cracks oriented perpendicular to σ_3 (e.g. Emerman and Marret, 1990), alignments of monogenetic centers can be used to trace back the stress arrangement prevailing at the

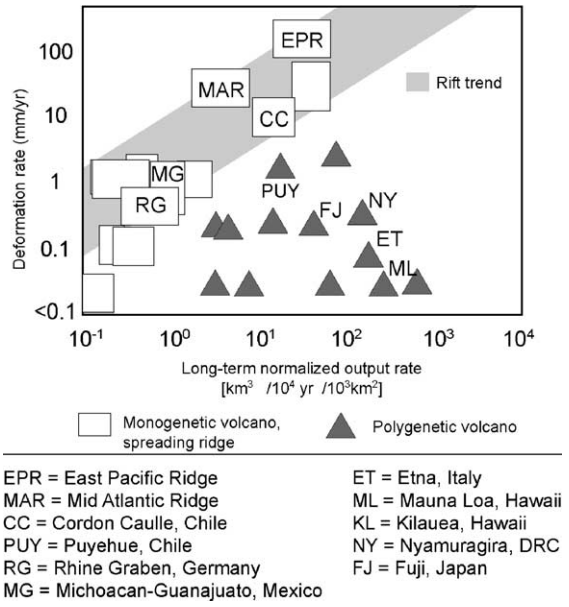

Fig. 12. Output rate vs. deformation rate diagram (Takada, 1994) showing good correlation between Cordón Caulle and the rift trend defined by monogenetic fields and spreading ridges, all developed under extensional settings. Output and deformation rates are shown for some volcanoes.

time of the eruption. In this context, NW-aligned pumice cones of Cordón Caulle would be consistent with extension (σ_2 and σ_3 horizontal) with σ_3 NE-oriented. We argue that given the high normalized output rate of silicic volcanism at Cordón Caulle, monogenetic volcanism can be used as an indication of high differential stress associated with intra-arc extension.

Because differential stress cannot be obtained directly, Takada (1994) used crustal displacement rates as a proxy of the differential stress. At Cordón Caulle, the relevant crustal displacement is that associated with extension, being partly accommodated by vertical movements including normal faulting and subsidence. As stated earlier, geochronological data of the Puyehue Volcano is used as reference for the timing of silicic volcanism at Cordón Caulle, which is combination with our gravity model, yields long-term subsidence rates of 1.5 cm/year (500 m/3.5×10^5 year). Interferometric Synthetic Aperture Radar (InSAR)-based data collected between the years 1993 and 1999 showed potential subsidence with an amplitude of several cm at Cordón Caulle (Pritchard and Simons, 2004; about 3 cm/year). Although InSAR measurements do not necessarily account for long-term subsidence rates, we stress the preliminary agreement between InSAR data and gravity regarding the nature of the deformation. Inferred deformation rates and normalized output rates of Cordón Caulle are plotted in Fig. 12, showing good correlation with monogenetic fields in extensional settings. Besides the negative gravity anomaly and the monogenetic style of volcanism, the flat-topped morphology of the depression is also a strong indication of extension.

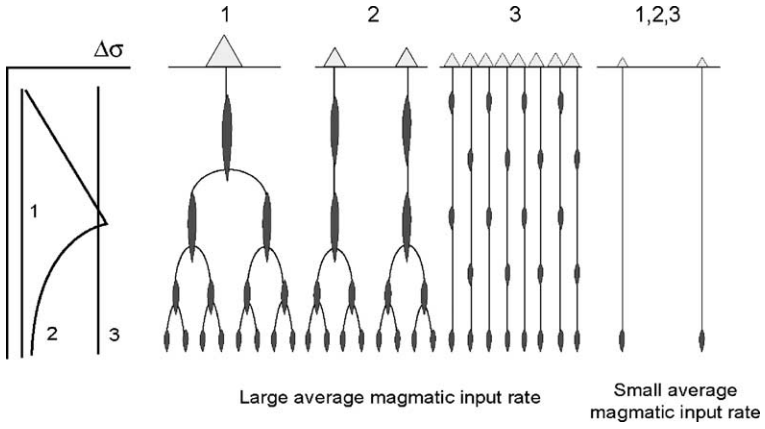

Fig. 13. Schematic representation of the crack coalescence theory (Takada, 1994). Escenario 3 corresponds to a monogenetic field formed under high output rates (proportional to magmatic input) and high differential stress, which is likely to be the case of Cordón Caulle during the period of felsic volcanism.

In his argumentation, Takada (1994) did not take into account the potential effect of the composition of the magmas in the estimation of normalized output rates. Because of their high viscosity, silicic magmas have limited ability to flow compared to basaltic magmas, and therefore, normalized output rates of rhyolitic magmas will tend to be lower than those of basaltic magmas, for equal erupted volumes and stress state. We believe that the high normalized output rate of felsic volcanism estimated for Cordón Caulle is in part reflecting this compositional effect.

The hypothesis of Cembrano and Moreno (1994) that evolved lavas of Cordón Caulle resulted from localized compression, given the orientation of NW-trending domains with respect to the prevailing Quaternary stress state (i.e. dextral transpressional with σ_1 NE-oriented), point, in conjunction with our interpretation of extension, to the coexistence of compressional and extensional regimes at Cordón Caulle. We interpret this apparent stress duality in terms of the Andean earthquake deformation cycle (Klotz et al., 2001), according to which extension is related to *coseismic* and *postseismic* deformation, and transpression is related to *interseismic* deformation (Fig. 13). During coseismic pulses, stress that is built up over tens to hundreds of years at locked subduction zones is released through elastic rebound of the overriding plate, resulting in both net displacement along the interplate contact and instantaneous extension (Fig. 13).

Insight into historic coseismic extension is provided by the great 1960 Chilean earthquake, with an inferred thrust faulting mechanism (Cifuentes, 1989), and slip distributed within a 900 km long, 150 km wide, margin-parallel rupture zone (Barrientos and Ward, 1990; Fig. 14). From the slip distribution and a static propagator technique, Barrientos (1994) concluded that coseismic deformation induced by the

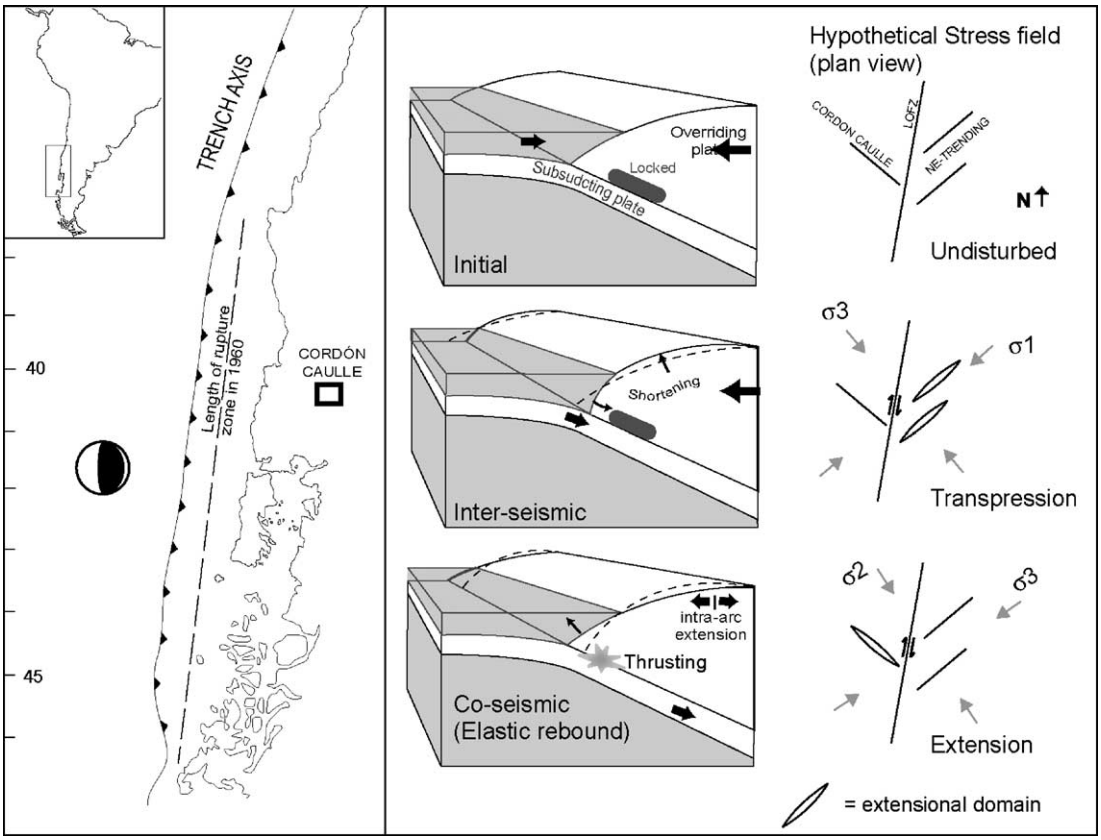

Fig. 14. Hypothetical coseismic and interseismic cycles of deformation along the intra-arc deformation zone.

1960 thrust event propagated inland triggering instantaneous, nearly east-west intra-arc extension. A particular effect of this would have been the 1960 eruption of Cordón Caulle, which started indeed 2 days after the earthquake. Coseimic extensional events could occur with a recurrence interval similar to that inferred for 1960 Chilean earthquake-type events (of 350–500 year; Barrientos and Ward, 1990; Madariaga, 1998).

Associated with the 1960 eruption, Lara et al. (2004) identified new-formed N20°/30 °W trending fissure vents. The exact direction of the minimum horizontal principal stress (i.e. σ_3) induced by the 1960 thrust was only semi-quantitatively constrained by Barrientos (1994), but the orientation of these breaching zones suggests that instantaneous extension occurred roughly in the same direction of plate convergence but in the opposite sense (i.e. N78°E). For σ_3 oriented N78°E, a component of dextral reactivation along the Cordón Caulle fissure could be also expected (Lara et al., 2004). Dextral kinematic indicators have not been documented along the Cordón Caulle fissure, but a number of Pliocene-Quaternary NW-striking dextral and also nearly N-S striking normal faults have been found all along the forearc zone, in northern Chile, and attributed to coseismic extensional deformation (González et al., 2003).

Based on the large magnitude of the 1960 thrust event, Klotz et al. (2001) attributed the non-uniform distribution of GPS-derived velocity vectors of the overriding plate between 37–42°S, to the continuing effect of the 1960 earthquake. Within this framework, InSAR data of Pritchard and Simons (2004) could be also interpreted in terms of post-seismic deformation following the 1960 earthquake, indicating that the interseismic regime has not been recovered in this region of the SVZ. Present-day subsidence at Cordón Caulle could be also linked to local post-eruptive effects of the 1960 eruption or geothermal activity.

6.2. Reactivation of the LOFZ

Intrusion INT crops out bracketed between the branches of the LOFZ in a prominent pop-up structure (Fig. 2), suggesting that reverse reactivation was the driving mechanism for basement exhumation in this area. In this section, we examine the conditions required for reverse reactivation of a high-angle fault such as the LOFZ. In particular, we consider the Late-Miocene to Pliocene (8.2–1.6 Ma) stress field of

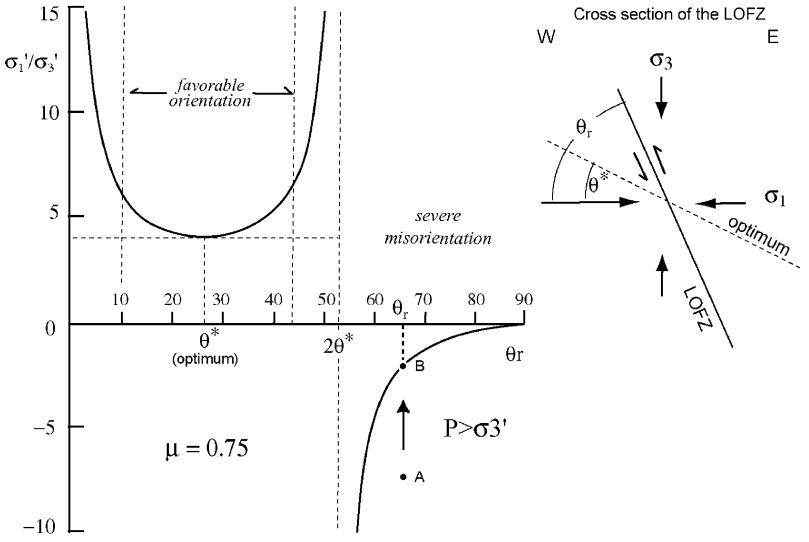

Fig. 15. Criteria for fault reactivation (Sibson, 1985). Path from A to B illustrates the effect of increasing fluid pressure over σ'_1/σ'_3 for a fault severely misoriented to the prevailing stress state. Point B describes fault reactivation; (B) Hypothetical eastwest cross section showing the orientation of the LOFZ to the Late Miocene-early Pliocene (before approximately 3.6 Ma) stress state (Lavenu and Cembrano, 1999), for an inferred θ_r (angle of reactivation)=65°.

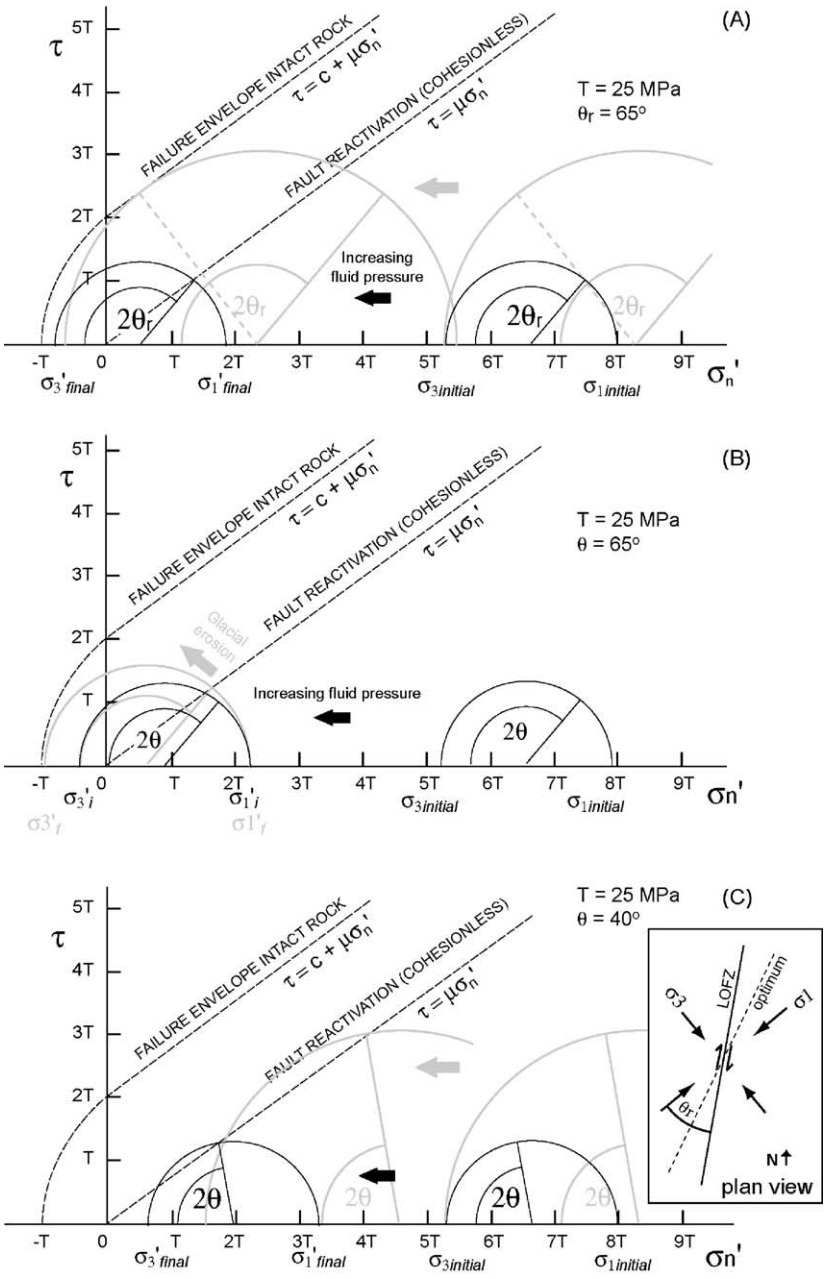

Fig. 16. (A) Estimation of fluid pressure required for new-formed reverse faults and reverse reactivation of the LOFZ, under a compressional stress state, for selected T=25 MPa, μ=0.75, θ_r=65° and depth=5 km (fixing $\sigma_{3\text{initial}}$ at 132 MPa or 5.3 T). In the case of high initial differential stress (here σ_1–σ_3=150 MPa or about 6 T, in gray), the fluid pressure increment (P_f) required for a new-formed fault is 152 MPa (λ=1.2; from Eq. (13) and that for fault reactivation is 178 MPa (λ=1.4; from Eq. (14). Fault reactivation is favored only by low initial differential stresses (σ_1–σ_3<80 MPa). (B) The effect of glacial denudation (in gray) combined with enhanced fluid pressure (in black), as a powered mechanism for reverse reactivation under a compressional stress state. In the example, a reduction of σ_3 (lithostatic load) of about 1/2 T (~10 MPa=0.1 kbar=350 m) will lead to fault reactivation, representing a period of 230,000 yr for a glacial denudation rate of 1.5 mm/year (~1.7 mm/year calculated in locality of sample PUY, see text); (C) the effect of increasing fluid pressure over the LOFZ, under a transpressional stress state (assumed σ_1 direction=N50°E). Note that dextral reactivation will be dominant over a wide range of initial stresses, due to the favorable orientation of the LOFZ (θ_r=40°; Fig. 10). Stress states taken from Lavenu and Cembrano (1999) and T=tensile strength taken from Lockner (1995).

compression with σ_1 oriented E-W, inferred from Lavenu and Cembrano (1999). If a fluid pressure P_f is present such as $\sigma'_i = \sigma_i - P_f$ is the effective principal stress i ($i = 1, 2, 3$), fault reactivation criteria can be expressed as a function of the ratio of the effective principal stresses as:

$$\frac{\sigma'_1}{\sigma'_3} = \frac{1 + \mu\cot\theta_r}{1 - \mu\tan\theta_r} \quad (12)$$

where θ_r is the orientation angle of an existing plane with respect to the σ_1 direction and μ is the coefficient of internal friction ($\mu = 0.75$ typical; Sibson, 1985, 1990). For the case of the LOFZ, we assume an overall N-S strike and $\theta_r = 65^\circ$ (Fig. 15). Following Eq. (12), a necessary condition for the reverse reactivation of the LOFZ would be $\sigma'_3 < 0$ or $P_f > \sigma_3$, or $\lambda = P_f/\sigma_3 > 1$, where λ is the pore fluid pressure factor (e.g.. Sibson, 2000) and $\sigma_3 = \rho g z$. Cycles of enhanced fluid pressure are supported by the close spatial relationship of the LOFZ with Late-Miocene intrusions, Quaternary volcanoes, and fossil and active hydrothermal activity. In the vicinity of sample INT, structurally-controlled hydrothermal alteration has been also observed.

We estimate the effective stresses that meet the criteria for reverse reactivation and formation of new reverse faults, for a given initial differential stress condition, using the relationship of effective stresses:

$$\sigma'_1 + \sigma'_3 = \frac{\Delta\sigma'(\sin 2\theta^* + \mu\cos 2\theta^*) - 2C}{\mu} \quad (13)$$

for reverse faulting, where θ^* is the optimum angle for reverse faulting ($\theta^* = 27^\circ$ for $\mu = 0.75$), $\Delta\sigma'$ is the effective differential stress ($\sigma'_1 - \sigma'_3$), which is known from the initial differential stress, and C is cohesion (e.g. 50 MPa; Lockner, 1995). For fault reactivation ($C = 0$), Eq. (13) reduces to:

$$\sigma'_1 + \sigma'_3 = \frac{\Delta\sigma'(\sin 2\theta_r + \mu\cos 2\theta_r)}{\mu} \quad (14)$$

where θ_r is as defined in Eq. (12). Comparison of initial and final stresses (Fig. 16) obtained from Eqs. (13) and (14) allow estimation of the increment in fluid pressure required for faulting. We use 200 MPa as the upper limit of crustal differential stress (Molnar and England, 1990), and neglect changes of μ and C with depth within the topmost 10 km. Within this vertical range, we conclude that the reactivation of the LOFZ is more likely to occur under low initial differential stress (>80 MPa). At differential stress greater than 80 MPa but lower than 100 MPa, hydraulic faults are more favorable to occur relative to reverse reactivation because they require a smaller increment of fluid pressure. At differential stresses greater than 100 MPa, reverse faults will be the most likely to occur (Fig. 16(A)).

Thomson (2002) attributed exhumation to the combined process of rock uplift induced by transpression and high erosion rates induced by glacial activity. Removal of lithostatic load (i.e. σ_3) induced by glacial erosion may have combined with fluid pressure to trigger reverse reactivation, by increasing the effective differential stress $\sigma'_1 - \sigma'_3$, provided that initial differential stress is low (Fig. 16(B)). Glacial denudation rates have been as rapid as 1.6 mm/year in the locality of sample PUYEHUE (age 310 ± 20 ka; 500 m high glacial scarpment). Glacial activity is thought to have potentially influenced the reactivation of the LOFZ since the Early-Pliocene at least. Glacial records in the SVZ include till formed sometime between approximately 7 and 4.2 Ma in the Patagonia (~47°S; Mercer and Sutter, 1982), and till interbedded with lavas (1.36–1.32 Ma old) of the Tronador Volcano (~41°S), the latter being correlated with the *Greatest Patagonian Glaciation* (Clapperton, 1993).

The 2D-analysis of Sibson (1985) predicts pure dextral strike-slip reactivation of the LOFZ during the Quaternary transpressional stress regime (Lavenu and Cembrano, 1999), for a wide range of initial differential stresses (Fig. 16(C)). Pure dip-slip induced by E-W compression and pure strike-slip induced by NE-SW transpression are theoretical scenarios which probably never occurred alone in nature. An oblique component of slip (and exhumation) is likely to have been present at all the stages of reactivation of the LOFZ.

7. Concluding remarks

Due to the lack of kinematic indicators, a multiple approach including gravity, thermochronology, geobarometry and morphology is attempted to explore the structural setting of the Cordón Caulle geothermal region. Cordón Caulle corresponds to NW-trending

volcano-tectonic depression characterized by a negative Bouguer anomaly, which is explained by a ~500 m thick infill of silicic lavas and tephra averaging 2000 kg/m^3 with respect to a background value of 2650 kg/m^3. Gravity data, together with the plateau-like morphology, the monogenetic style of volcanism, and the orientation of breaching zones associated with the 1960 eruption, are indicative of extension. Previous workers have inferred a compressional behavior at Cordón Caulle, based on the occurrence of silicic volcanism and the orientation of Cordón Caulle with respect to the well-documented Quaternary dextral transpressional state. We argue that a dual stress regime is consistent with the earthquake cycle dominating crustal deformation. At Cordón Caulle, periods of inter-seismic elastic shortening in the direction of plate convergence would favor magma stagnation and differentiation, and periods of coseismic deformation induced by large-scale earthquakes would induce extension. During the late Miocene-Pliocene (8.2–1.6 Ma), the intra-arc stress field was given by E-W compression. For this stress field, conditions of enhanced magmatic-hydrothermal fluid pressure, low differential stress and rapid removal of lithostatic load by glacial erosion, allow to anticipate a component of reverse reactivation of the LOFZ. In the vicinity of Cordón Caulle, a portion of the crystalline basement crops out confined to the branches of the LOFZ in a prominent pop-structure, in agreement with the premise of reverse reactivation. In this area, basement exhumation rates are estimated to be greater than 1 mm/year.

Acknowledgments

The authors would like to thank CONICYT (National Council of Science and Technology, CHILE) for financial support through the FONDEF Grant No. 1051 “Characterization and Assessment of Geothermal Resources of Central and Southern Chile: Possibilities of Generation of Electric Energy and Direct Applications”. Thanks are extended to Carlos Palacios, Mauricio Belmar, Miguel A. Parada, Sofia Rebolledo (Department of Geology, University of Chile); Carlos Pérez de Arce, Luis Lara (National Geological Survey, SERNAGEOMIN); Javier Labra and Nicolás Pacheco (CONAF National Park Puyehue, CHILE); and Supri Soengkono (Geothermal Institute of the University of Auckland, New Zealand; designer of GRAV2D-Win Software).

References

Aguirre, L., Levi, B., 1964. Geología de la Cordillera de los Andes de las Provincias de Cautín, Valdivia, Osorno y Llanquihue. Boletín, vol. 17. Instituto de Investigaciones Geológicas, Chile. 37 pp.

Anderson, J.L., Smith, D.R., 1995. The effects of temperature and fO_2 on the Al in hornblende barometer. American Mineralogist 80, 549–559.

Angermann, D., Klotz, J., Reigber, C., 1999. Space-geodetic estimation of the Nazca–South America Euler vector. Earth and Planetary Science Letters 171, 329–334.

Araneda, M., Avendaño, M.S., Schmidt, S., Götze, H., Muñoz, J., 1999. Hoja Puerto Montt: Carta gravimétrica de Chile. Subdirección Nacional de Geología. SERNAGEOMIN, CHILE. 16 pp.

Barrientos, S., 1994. Large thrust earthquakes and volcanic eruptions. PAGEOPH 142, 225–237.

Barrientos, S., Ward, S.N., 1990. The 1960 Chile earthquake: inversion for slip distribution form surface deformation. Geophysical Journal International 103, 589–598.

Blundy, J.D., Holland, T.J.B., 1990. Calcic amphibole equilibria and a new amphibole–plagioclase geothermometer. Contributions to Mineralogy and Petrology 104, 208–224.

Cahill, T., Isaacks, B., 1992. Seismicity and shape of the subducted Nazca Plate. Journal of Geophysical Research 97, 17503–17529.

Campos, A., Moreno, H., Muñoz, J., Antinao, J., Clayton, J., Martín, M., 1998. Mapa Geológico del Área de Futrono (1:1.000.000). Servicio Nacional de Geología Minería, CHILE.

Cembrano, J., Moreno, H., 1994. Geometría y naturaleza contrastante del volcanismo cuaternario entre los 38° y 46 °S: dominios compresionales y tensionales de un régimen transcurrente? 7° Congreso Geológico Chileno 1, 240–244.

Cembrano, J., Hervé, F., Lavenu, A., 1996. The Liquiñe–Ofqui fault: a long-lived intra-arc fault system in southern Chile. Tectonophysics 259, 55–66.

Cembrano, J., Schermer, E., Lavenu, A., Sanhueza, A., 2000. Contrasting nature of deformation along an intra-arc shear zone, the Liquiñe–Ofqui fault zone, Southern Chilean Andes. Tectonophysics 319, 129–149.

Cembrano, J., Lavenu, A., Reynolds, P., Arancibia, G., López, G., Sanhueza, A., 2002. Late Cenozoic transpressional ductile deformation north of the Nazca–South America–Antartica triple junction. Tectonophysics 354, 289–314.

Cifuentes, I., 1989. The 1960 Chilean earthquakes. Journal of Geophysical Research 94 (B1), 665–680.

Clapperton, C., 1993. Quaternary Geology and Geomorphology of South America. Elsevier Science Publishers, Amsterdam. 779 pp.

Dixon, H.J., Murphy, M.D., Sparks, S.J., Chávez, R., Naranjo, J.A., Dunkley, P.N., Young, S.R., Gilbert, J.S., Pringle, M.R., 1999.

The geology of the Nevados de Chillán volcano, Chile. Revista Geológica de Chile 26 (2), 227–253.
Emerman, S., Marret, R., 1990. Why dikes? Geology 18, 231–233.
Forsythe, R., Nelson, E., 1985. Geological manifestations of ridge collision: evidence from the Golfo de Penas–Taitao Basin, southern Chile. Tectonics 4, 477–495.
Gerlach, D., Frey, F., Moreno, H., López-Escobar, L., 1988. Recent volcanism in the Puyehue–Cordón Caulle region, Southern Andes, Chile (40, 5° S): petrogenesis of evolved lavas. Journal of Petrology 29 (2), 333–382.
González, G., Cembrano, J., Carrizo, D., Macci, A., Schneider, H., 2003. The link between forearc tectonics and Pliocene-Quaternary deformation of the Coastal Cordillera, northern Chile. Journal of South American Earth Sciences 16, 312–342.
Hammarstrom, J.M., Zen, E., 1986. Aluminum in hornblende: an empirical igneous geobarometer. American Mineralogist 71, 1297–1313.
Harper, M.A., Singer, B.S., Moreno, H., Lara, L., Naranjo, J., 2004. $^{40}Ar/^{39}Ar$ constraints on the evolution of the Puyehue-Cordón Caulle Volcanic Complex, Andean Southern Volcanic Zone, Chile. Abstracts IAVCEI General Assembly, Symposium 12b.
Hollister, L.S., Grissom, G.C., Peters, E.K., Stowell, H.H., Sisson, V.B., 1987. Confirmation of the empirical correlation of the Al in hornblende with pressure of solifification of calc-alkaline plutons. American Mineralogist 72, 231–239.
Johnson, M.C., Rutherford, M.J., 1989. Experimental calibration of the aluminum-in-hornblende geobarometer with application to Long Valley caldera (California) volcanic rocks. Geology 17, 837–841.
Klotz, J., Khazaradze, G., Angermann, D., Reigber, C., Perdomo, R., Cifuentes, O., 2001. Earthquake cycle dominates contemporary crustal deformation in Central and Southern Andes. Earth and Planetary Science Letters 193, 437–446.
Lahsen, A., 1978. Características Geoquímicas y Origen de Las Aguas Termales de Chillán, Comunicaciones. Dep. de Geol., Univ. De Chile, pp. 35–48.
Lara, L., Rodríguez, C., Moreno, H., Pérez de Arce, C., 2001. Geocronología K-Ar y geoquímica del volcanismo plioceno superior-pleistoceno de los Andes del Sur (39°–42 °S). Revista Geológica de Chile 28 (1), 67–90.
Lara, L., Moreno, H., Naranjo, J., 2004. Rhyodacitic fissure eruption in Southern Andes (Cordón Caulle; 40.5 °S) after the 1960 (Mw:9.5) Chilean earthquake: a structural interpretation. Journal of Volcanology and Geothermal Research 138, 127–138.
Lavenu, A., Cembrano, J., 1999. Compressional and transpressional-stress pattern for Pliocene and Quaternary brittle deformation in fore and intra-arc zones (Andes of Central and Southern Chile). Journal of Structural Geology 21, 1669–1691.
Leake, B., Wooley, A., Arps, C.E.S., Birch, W.D., Gilbert, M.C., Grice, J.D., Hawthorne, F.C., Kato, A., Kisch, H.J., Krivovichev, V.G., Linthout, K., Laird, J., Mandarino, J.A., Maresch, J.C., Schumacher, J.C., Smith, D.C., Stephenson, N.C.N., Ungaretti, L., Whittaker, E.J.W., Youzhi, G., 1997. Nomenclature of amphiboles: report of the subcommittee on amphiboles of the international mineralogical association, commission of new minerals and mineral names. Canadian Mineralogist 35, 219–246.
Lockner, D.A., 1995. Rock failure. In: Ahrens, T.J. (Ed.), Rock Physics and Phase Relations: A Handbook of Physical Constants, American Geophysical Union Reference Shelf, 3, pp. 127–147.
Longman, I.M., 1959. Formulas for computing the tidal acceleration due to the moon and the sun. Journal of Geophysical Research 64, 2351–2355.
López-Escobar, L., Cembrano, J., Moreno, H., 1995. Geochemistry and tectonics of the Chilean Southern Andes basaltic Quaternary volcanism (37°–46 °S). Revista Geológica de Chile 22 (2), 219–234.
Madariaga, R., 1998. Sismicidad de Chile. In: Buforn, E., Udías, A. (Eds.), Física de la Tierra, Sismicidad de Centro y Sudamérica. Servicio de Publicaciones Universidad Complutense, Madrid, pp. 221–258. N°10.
Mercer, J.H., Sutter, J.F., 1982. Late Miocene-Earliest Pliocene glaciation in Southern Argentine: implications for gloal ice-sheet history. Palaeogeography, Palaeoclimatology, Palaeoecology 38, 185–206.
Molnar, P., England, P., 1990. Temperatures, heat flux, and frictional stress near major thrust faults. Journal of Geophysical Research 95, 4833–4856.
Moreno, H. 1977. Geología del área volcánica de Puyehue-Carrán en los Andes del sur de Chile. Memoria de Título, Universidad de Chile, Departamento de Geología, Santiago. 170 pp.
Munizaga, F., Hervé, F., Drake, R., Pankhurst, R.J., Brook, M., Snelling, N., 1988. Geocronology of the Lake Region of south-central Chile (39°–42 °S): preliminary results. Journal of South American Earth Sciences 1 (3), 309–316.
Otten, M.T., 1984. The origin of brown hornblende in the Artfjället gabbro and dolerites. Contributions to Mineralogy and Petrology 86, 189–199.
Parada, M.A., Lahsen, A., Palacios, C., 2000. The Miocene plutonic event of the Patagonian Batholith at 44°30′: thermocronological and geobarometric evidence for melting of a rapidly exhumated lower crust. Transactions of the Royal Society of Edinburgh. Earth Sciences 91, 169–179.
Pardo-Casas, F., Molnar, P., 1987. Relative motion of the Nazca (Farallon) and South American plates since the Late Cretaceous times. Tectonics 6, 233–248.
Pérez, Y., 1999. Fuentes de Aguas Termales de la Cordillera Andina del Sur de Chile (39°-42 °S). Subdirección Nacional de Geología, Boletín, vol. 54. SERNAGEOMIN, CHILE.
Pérez de Arce, C., Becker, T., Roeschmann, C., 2000. El nuevo sistema de datación $^{40}Ar/^{39}Ar$ equipado con láser de CO_2 en el Sernageomin. IX Congreso Geológico Chileno 1, 675.
Pérez de Arce, C., Matthews, S., Klein, J., 2003. Geochronology by the $^{40}Ar/^{39}Ar$ method at the Sernageomin Laboratory, Santiago, Chile. Internacional Conference on Research Reactor Utilization, Safety, Decommissioning, Fuel and Waste: Extended Synopsis, pp. 82–83.
Pritchard, M.E., Simons, M., 2004. An InSAR-based survey of volcanic deformation in the Southern Andes. Geophysical Research Letters 31, LI5610.
Renne, P., Deino, A.L., Walter, R.C., Turrin, B.D., Swisher, C.C., Becker, T.A., Curtis, G.H., Sharp, W.D., Jaouni, A., 1994. Inter-

calibration of astronomical nad radioisotopic time. Geology 22, 783–786.

Schmidt, M.W., 1992. Amphibole composition in tonalite as a function of pressure: and experimental calibration of the Al-in-hornblende barometer. Contributions to Mineralogy and Petrology 110, 304–310.

Sepúlveda, F., Lahsen, A., 2003. Geothermal exploration in Central-Southern Chile. Geothermal Resources Council, Transactions 27, 635–638.

Sepúlveda, F., Dorsch, K., Lahsen, A., Bender, S., Palacios, C., 2004a. The chemical and isotopic composition of geothermal discharges from the Puyehue–Cordón Caulle area (40.5 °S), Southern Chile. Geothermics 33/5, 655–673.

Sepúlveda, F., Lahsen, A., Dorsch, K., Palacios, C., 2004b. Chemistry of fumaroles from the Cordón Caulle geothermal region, Southern Chile. Abstracts IAVCEI General Assembly, Symposium 10a.

Sibson, R., 1985. Short notes: a note on fault reactivation. Journal of Structural Geology 7 (6), 751–754.

Sibson, R., 1990. Rupture nucleation on unfavorably oriented faults. Bulletin of Seismological Society of America 80 (6), 1580–1604.

Sibson, R.H., 2000. A brittle failure mode plot defining conditions for high-flux flow. Economic Geology 95, 41–48.

Somoza, R., 1998. Updated Nazca (Farallon)–South America relative motions during the last 40 My: implications for mountain building in the central Andean region. Journal of South American Earth Sciences 11, 211–215.

Spear, F.S., 1981. Amphibole-plagioclase equilibria: an empirical model for the relation albite+tremolite=edenite+4 quartz. Contributions to Mineralogy and Petrology 77, 355–364.

Takada, A., 1994. The influence of regional stress and magmatic input on styles of monogenetic and polygenetic volcanism. Journal of Volcanology and Geothermal Research 99 (B7), 13563–13573.

Talwani, M., Worzel, J.L., Landisman, M., 1959. Rapid gravity computations for two dimensional bodies with application to the Mendocino submarine fracture zone. Journal of Geophysical Research 64, 49–59.

Tassara, A., 1997. Segmentación andina desde el análisis flexural de la anomalía de Bouguer. Unpub. M.Sc. Thesis, Universidad de Chile. 140 pp.

Tassara, A., Schmidt, S., Tasarova, Z., Hackney, R., Wienecke, S., Götze, H.J., 2004. Structure, composition and thermomechanical state along the segmented Andean margin. Abstracts IAVCEI General Assembly, Symposium 8f.

Thomson, S.N., 2002. Late Cenozoic geomorphic and tectonic evolution of the Patagonian Andes between latitutes 42 °S and 46 °S: an appraisal based on fission-tracks results from the transpressional intra-arc Liquiñe–Ofqui fault zone. Geological Society of America Bulletin 114 (9), 1159–1173.

Torge, W.T., 1989. Gravimetry. In: de Gruyter, W. (Ed.), New York, 465 p.